REPORT DOCUMENTATION PAGE

1. REPORT DATE *(DD-MM-YYYY)*	2. REPORT TYPE	3. DATES COVERED *(From - To)*
6/03/14	Final Technical Report	December 21, 2009 - February 29, 2012

4. TITLE AND SUBTITLE

Autonomous Sensor Motes Employing Liquid-Bearing Rotary Stages

5a. CONTRACT NUMBER

5b. GRANT NUMBER

W31P4Q-10-1-0002

5c. PROGRAM ELEMENT NUMBER

6. AUTHOR(S)

Ming C. Wu (PI)
Bernhard Boser (Co-PI)
David Horsley (Co-PI)

5d. PROJECT NUMBER

5e. TASK NUMBER

5f. WORK UNIT NUMBER

7. PERFORMING ORGANIZATION NAME(S) AND ADDRESS(ES)

University of California, Berkeley
Sponsored Projects Office
2150 Shattuck Ave. Suit 300
Berkeley, CA 94704-5940

8. PERFORMING ORGANIZATION REPORT NUMBER

9. SPONSORING/MONITORING AGENCY NAME(S) AND ADDRESS(ES)

US ARMY Contracting Command
RDEC Contracts Division A/CCAM-RD-A
(Attn: Deborah Blackburn, 256-842-7567)
Redstone Arsenal, AL 35898-5280

10. SPONSOR/MONITOR'S ACRONYM(S)

11. SPONSOR/MONITOR'S REPORT NUMBER(S)

12. DISTRIBUTION/AVAILABILITY STATEMENT

Approved for public releases, distribution unlimited

13. SUPPLEMENTARY NOTES

14. ABSTRACT

The liquid bearing technology provides a self-centering, friction and wear resistant bearing capable of supporting static and dynamic loads. The liquid bearing design uses satellite droplets arranged around a central droplet. The satellite droplets are pinned to the rotor by patterning of the hydrophobic surface coating, but slide across the stator's hydrophobic coating. The center droplet maintains alignment between the rotor and stator. Experimental data and models demonstrate the performance and stability of the design. Superhydrophobic coatings are required to successfully retain the satellite droplets on the rotor and to permit sliding of the droplets across the stator surface. The satellite droplet liquid bearing was characterized to have minimum startup torque at 0.3 µN-m, rotational drag coefficient at $0.94 \cdot 10^{-3}$ µN-m/rpm, and maximum rotation rate at 14400 deg/sec for an input torque of 2.3 µN-m. The tilt stiffness of the satellite bearing design was measured at 5.4 µN-m/deg. Tilt stiffness measurement and analytical models provide the design tools needed for predicting pull-in instability threshold gaps and voltages.

15. SUBJECT TERMS

Liquid bearing, micromotor, surface tension, friction reduction, wear resistant, superhydrophobic coating

16. SECURITY CLASSIFICATION OF:			17. LIMITATION OF ABSTRACT	18. NUMBER OF PAGES	19a. NAME OF RESPONSIBLE PERSON
a. REPORT	b. ABSTRACT	c. THIS PAGE			USARME
U	U	U	UU	55	19b. TELEPHONE NUMBER *(Include area code)*

Reset

Final Technical Report

Project Title:

Autonomous Sensor Motes
Employing Liquid-Bearing Rotary Stages

Award Number:

ONR W31P4Q-10-1-0002

PI:

Ming C. Wu
University of California, Berkeley

Co-PIs:

David Horsley, UC Davis
Bernhard Boser, UC Berkeley

Table of Contents

1. Liquid Bearing Supported Rotary Motor: Background

1.1 Background

Micro-ElectroMechanical Systems (MEMS) are energy transducers, converting energy and signals between mechanical and electrical domains. MEMS sensors translate mechanical phenomena, such as position, velocity, acceleration, pressure, or force, into electrical signals; MEMS actuators translate electrical signals into mechanical phenomena. This work aims to improve the function and capability of MEMS rotary actuators through development of a novel liquid bearing technology.

Early MEMS rotary micromotors suffered from friction issues limiting their capability and useful lifetime: devices such as center-pinned, electrostatic wobble motors [1, 2], ultrasonic [3, 4] and magnetic [5] drive motors. Numerous attempts to alleviate fiction in rotary devices have been presented, including micro-ball bearings [6], externally pressurized, dynamic air bearings [7], and contact-free bearings created by electrostatic or magnetic suspension [8, 9], but these efforts either maintained solid-solid contact, operate in a limited range, or require actively controlled components. McCarthy *et al* [10] provide a detailed discussion of the advantages and short-comings of various rotary micromotor support techniques.

The liquid bearing technology developed in this work provides a self-centering, friction and wear resistant bearing capable of supporting static and dynamic loads. The liquid bearing design uses satellite droplets arranged around a central droplet, shown in Fig. 1. The satellite droplets are pinned to the rotor by patterning of the hydrophobic surface coating, but slide across the stator's hydrophobic coating. The center droplet maintains alignment between the rotor and stator. Experimental data and models demonstrate the performance and stability of the design. Superhydrophobic (SHP) coatings are required to successfully retain the satellite droplets on the rotor and to permit sliding of the droplets across the stator surface. Design and selection of the SHP coatings are discussed and material properties characterized.

Magnetic drive similar to [5, 11] was used in testing the performance of the micromotor. Characterization of minimum torque requirements and maximum rotation rates for three liquid bearing designs (disk, ring and full bearings) using two fluids (water and ethylene glycol) demonstrated good agreement between measurement and rotational viscous friction models. Previous liquid bearings have been demonstrated [12-14], but were unstable in tip/tilt, or only developed stability when rotating at significant speeds. A critical requirement of successful bearing design is supporting out-of-plane loads and sufficient tip/tilt stability margin to accommodate forces and torques generated by the actuation system, particularly in the case of electrostatic snap-in instability. This work presents a liquid bearing design that is tip/tilt stable and characterizes stiffness to permit drive mechanism instability calculations.
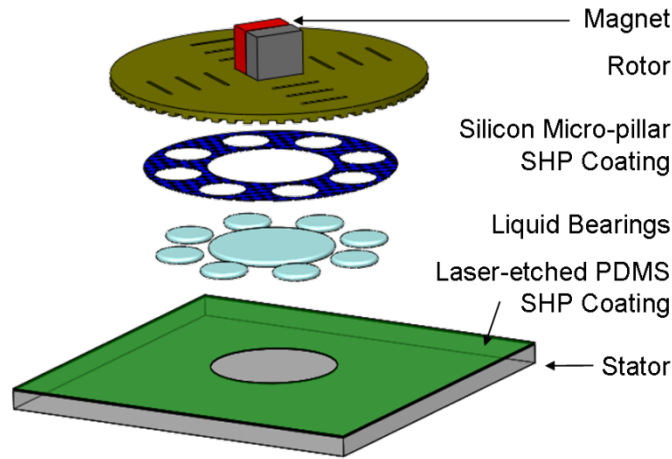
Fig. 1. Expanded schematic of the liquid bearing design demonstrated in this work. A silicon and cytop micro-pillar patterned superhydrophobic (SHP) coating on the rotor defines center and satellite liquid bearing droplets. A laser-etched, nano-featured PDMS SHP coating on the stator aligns the bearing to the stator.

1.2 Literature Review

1.2.1 MEMS Rotary Motors

In 1987, Trimmer *et al* [15] proposed design parameters for MEMS electrostatic micromotors, using fundamental theory to derive forces created in variable displacement capacitors and applying the calculations to elementary linear and rotary micromotor geometries. The goal of that work was to lay out the practical design considerations for development of micro-scale motors through silicon processing, and it serves as the basis for much of the work that has been done in the 24 years following.

Early fabrication of MEMS micromotors were reported at UC Berkeley Microfabrication Laboratory by Fan, Tai, and Muller [1, 16-18]. The devices were center pinned, stepping or synchronous motors based on variable capacitance, fabricated by deposition and surface micromachining of polysilicon, silicon oxide, and silicon nitride layers. The motor torques were on the order of a few pN-m, and methods such as bushings, silicon nitride spacers, and uncontrolled electrostatic levitation were used to counteract the friction effects. Coefficients of friction were experimentally determined for the solid-solid contact of polysilicon on silicon nitride and ranged from 0.21 to 0.38.

Mehregany *et al* [2, 19, 20] describe variable-capacitance, rotary, harmonic side-drive micromotors, or wobble motors. The wobble motors are fabricated from deposition and surface micromachining of low-temperature oxide (LTO) and doped polysilicon layers. In running tests to characterize bearing friction for the wobble motors, significant wear developed between the rotor and center pin, changing the clearance by as much as 25% over several million actuation cycles.

1.2.2   Friction Characterization

Numerous efforts have sought to quantify and characterize the friction and wear issues inherent in the solid-solid contact of MEMS micromotors. Lim *et al* [21] fabricated test structures allowing indirect measurement of fictional coefficients for polysilicon on silicon nitride or polysilicon. Normal forces were applied by electrostatic attraction, the friction force measured by pulling the sliding part with comb drive actuators. Frictional coefficient was determined by dividing the friction force by the applied normal force. The measured coefficients were higher than predicted and previous work, up to values of 2.5, partially due to interaction of the electrostatic attraction method of normal force application.

Beershwinger *et al* [22] provided a review of sliding coefficient of friction tests presented in the literature, and reported coefficients ranging from 0.2 to 1.8 for various IC-process-compatible materials. They then experimentally measured the static and dynamic friction coefficients for a variety of materials and loading conditions, replacing the electrostatic normal force application with micro-masses and gravity-based normal forces. The best performing materials were polysilicon sliding on either single crystal silicon or diamond like carbon which both had coefficients of 0.2. Additionally, microspheres were used as a bearing in an attempt to lower the friction by changing from sliding to rolling friction mechanisms, with measured friction coefficient of 0.05, a factor of 4 better than the best sliding measurements and a factor of about 10 better than the average of all the sliding material friction measurements. Although the microsphere bearings provided significantly improved friction performance, questions remained about their fabrication in situ and ease of use.

Zhang *et al* [23] looked at the root causes of friction and wear-induced failures in solid-solid contact in micro-actuators. Primary effects included fracture of the contacting surfaces, contamination by externally introduced particles or through the fracture of the surfaces, and the effects of stiction due to molecular level attractive forces. Suggested methods of improving friction were material selection, lubricating films, and lubricating fluids.

1.2.3   Friction Alleviation Efforts

1.2.3.1   Hydrostatic Journal Bearing

Hydrostatic Journal Bearings are externally pressurized fluid bearings that derive the ability to separate a rotor shaft from stator sleeve from the pressure distribution along fluid introduction ports when the gap between rotor and stator near the port is small. Several rotary micromotors have been demonstrated using fluid lubrication layers to reduce friction and wear. Piekos [24] models gas-lubricated dynamic journal bearing designs for application in micro-fabricated turbines used for power generation which operate at rotational speeds of millions of RPMs. Gas-lubricated bearings alleviate solid-solid friction concerns, but the models captured positioning instabilities as a function of geometry and rotation rate. Frechette *et al* [7] discuss fabrication and testing of a gas-lubricated bearing supported micro-turbine, showing stable, low-friction operation at 1.4 million RPM. Failure of the micro-turbines was demonstrated to occur via both high-speed instability and low-speed failure of journal bearing separation of the rotor and

stator. Ehrich *et al* [25] discuss other journal bearing designs that may increase the high-speed stability of the micro-turbine and demonstrate a test apparatus for development.

1.2.3.2   Hydrodynamic Journal Bearings

Hydrodynamic Journal Bearings are non-pressurized fluid bearings that derive the ability to separate a rotor shaft from stator sleeve via local pressure areas created by the rotor dragging fluid into the narrowest part of the gap between rotor and stator. Fluid dynamic bearings (FDB) incorporating oil to support hard disk drives are discussed by Matsuoka *et al* [26]. The FDB is a dual purpose bearing that operates as a thrust bearing and a radial, journal-type bearing. As with gas-bearings, the journal bearing operation of FDBs is limited at low rotation speeds. Asada *et al* [12] tested several FDB designs; the best design tested was a 5 mm diameter shaft with 5-15 μm clearance, with asymmetric herringbone grooves at 17° and was successfully operated at 20,000 rpm with no noticeable bubble mixing.

1.2.3.3   Actively Controlled Levitation

A number of methods have been investigated to extend the operating range of non-contact bearing designs to lower rotation rates than successfully demonstrated in gas and fluid lubricated bearings. These methods are typically actively controlled levitation of the rotor using a field. Wu *et al* [9] demonstrate a magnetically levitated rotor design based on a 10 MHz AC field, and achieve rotation rates up to 1400 RPM and the ability to withstand de-centering disturbances of up to 80 μm. Kumar *et al* [8] demonstrated a non-rotating, electrostatically-levitated rotor using an 8.16 MHz resonant field which sustained a 200 μm gap. Both demonstrated levitation methods require controlled and externally-powered field to maintain positional alignment in the contact-free bearing design. Fuhr *et al* [27] demonstrate levitation of a rotor based on electric field traps produced by application of AC electric fields. The unique characteristic of the Fuhr micromotor was incorporation of a high dielectric constant fluid into the gap between rotor and stator electrodes to increase the electrostatic force and reduce sensitivity to variations in the gap between electrodes.

1.2.3.4   Micro-ball Bearing

Recent design efforts to expand the operating range of rotary micro-machines to low RPM or static positioning has been done with the use of micro-ball bearings. Ghalichechian *et al* [6] demonstrate micro-ball bearings captured within silicon races that provide alignment stability at speeds from 0-517 RPM. The micro-ball bearings represent a compromise between reducing friction in the rotating machine and expanding the operating space to low frequencies.

Table 1 summarizes the types of friction reduction methods that have been developed to improve rotary micromotor performance regarding wear and lifetime. The designs are all demonstrated to relieve friction but are either limited in their operating range (hydrostatic and hydrodynamic pressure based fluid bearings) or have undesirable characteristics in their operation (powered and controlled operation or solid-solid contact between parts).

Table 1: Various bearing designs are compared in terms of their operating requirements (external power, control), friction issues (solid-solid contact), and range of rotation rates.

Bearing Type	Hydrostatic	Hydrodynamic	Electostatic	Magnetic	Micro-ball
Author	Frechette	Asada	Kumar	Wu	Ghalichechian, McCarthy
Powered	X		X	X	
Controlled			X	X	
Solid-Solid					X
Min Ω [rpm]	>1000?	>1000?	N/A	0	0
Max Ω [rpm]	1.4E+06	20000	N/A	1400	517

1.2.4   Magnetic Actuation of Rotary Micromotors

Wagner *et al* [11] demonstrated a rotating micromotor created with a permanent magnet on the rotor and magnetic field created by conductive coils on the stator, shown in Fig. 2. The rotor was a cylindrical Sm-Co magnet with diameter 1.4 mm and height 1.0 mm, and magnetization $M = 0.85$ T. The stator consisted of four coils fabricated by electroplating gold over a silicon nitride insulation layer, with line widths of 30 μm, spacing between lines of 20 μm, and thickness of 26 μm. Each of the four coils subtended an 80° arc, had five turns and electrical resistance of 1.4 Ω. A motor driven with 0.5 A in two opposite coils produced a maximum applied torque of 116 nN-m, and could be operated step-wise in 4 or 8 steps by powering combinations of coils.
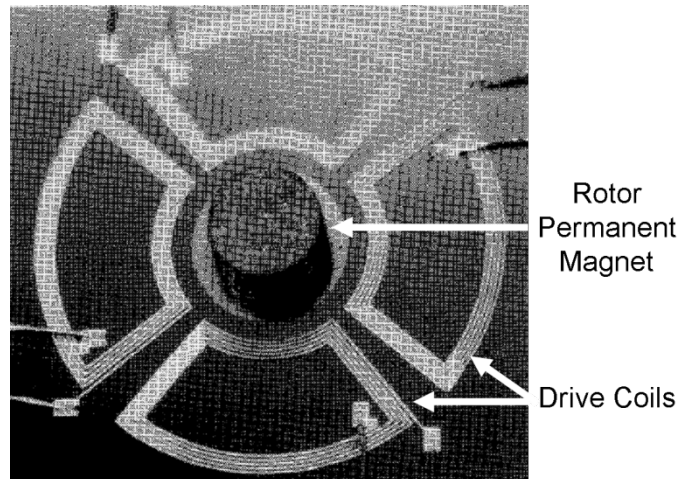

Fig. 2. Wagner *et. al.* permanent magnet motor using lithographically patterned coils on the glass stator. The magnet is retained in position using a glass slide (not visible) with an etched hole above the stator.

The rotor was maintained in position by a glass sheet above the stator that restricted translation to within the 500 μm clearance around the magnet. Minimum observed operating current was 130 mA, corresponding to a maximum torque of approximately 30 nN-m. The maximum operating speed for input current of 0.5 A was observed to be 2000 rpm. The motor had no friction reducing methods.

Lu *et al* [28] developed a variable reluctance magnetic motor that did not require a permanent magnet on the rotor to create driving torque, shown in Fig. 3. Instead, the motor relies on geometry of poles on the stator and rotor, using changes in gap and pole overlap to create the driving force. The device that was fabricated and tested had 12 stator poles and 10 rotor poles, allowing minimum step sizes of 12°. The rotor is supported on a center pin fabricated from polyimide. Predicted torque based on a change in inductance with angular position change is 3.3 nN-m. With drive inputs current at 200 mA, the motor was demonstrated to function in continuous rotation up to rates of 500 rpm.
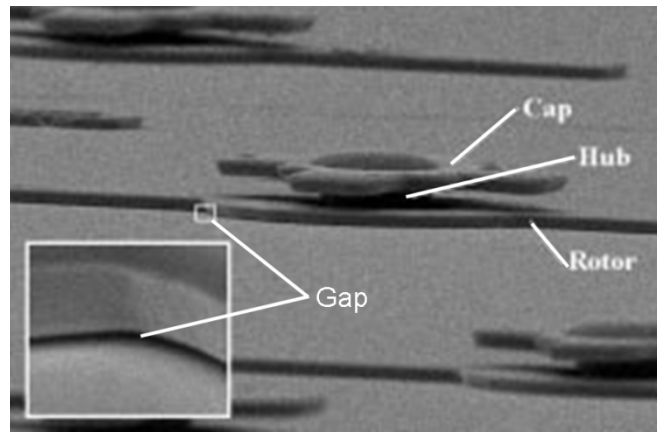

Fig. 3. Lu *et. al.* variable reluctance micromotor SEM image. The cap diameter is approximately 100 μm, the gap between rotor and substrate is on the order of micrometers.

1.2.5 Hydrophobic Surface Patterning for Droplet Retention

Darhuber *et al* [29] discuss a wide array of droplet positioning mechanisms that have been reported, including methods of controlled droplet flow in microchannels on glass or silicon. Modulation of the energy at fluid-fluid or fluid-solid contact boundaries is accomplished by several techniques including electrowetting [30-32], dielectrophoresis [33], and thermocapillary [34] action.

Many examples exist of surface patterning and surface tension being used to provide positional alignment between MEMS parts, specifically in the field of fluidic self assembly. Srinivasan *et al* [35, 36] created hydrophobic and hydrophilic regions on the substrate and microparts by oxidation and self-assembled monolayers respectively. During the assembly process, the hydrophobic surfaces were coated with an adhesive; the microparts were then pipetted towards a substrate submerged in water. The surface properties caused the microparts to align, and fill factors of up to 95% were demonstrated.

Abassi *et al* [37] demonstrated that although positional alignment often gave good results, the adhesive droplet between microparts and substrate often was volumetrically uneven, resulting in micropart tilt and variation between devices. By utilizing vibration in a direction perpendicular to the substrate, the tilt angle was shown to decrease, the result of driving the low energy resting position of the micropart to one parallel with the substrate.

1.2.6   Fluid Droplet Micro-Scale Devices

The use of fluid droplets as a critical mechanical part of MEMS devices has been somewhat less frequently documented. Takei *et al* and Kajiwara *et al* [13, 38] demonstrate a water droplet based micromotor driven by electrowetting on dielectric (EWOD). The Takei rotor was capable of rotating at 12 Hz. The Kajiwara motor operated at slightly more than 5Hz. In an EWOD motor, stator electrodes are patterned beneath a dielectric layer around the exterior edge of the fluid droplet. A large central electrode acts as an electrical ground. When a potential is applied to electrodes on the stator's exterior edge, the droplet deforms outwards near the active electrodes. The deformation of the droplet by the stator potential creates a minimum energy position for the rotor poles, which causes a rotational torque until the rotor poles are aligned to the active stator poles.

Lee *et al* [39] demonstrate a different rotary micromotor based on electrowetting droplets. In their effort, the droplets were mercury that travelled in a circumferential race, driven by electrowetting. A rotor could be driven by the droplets, though the authors do not discuss or demonstrate a coupling method.

1.3 Liquid Bearing Advantages

The liquid bearing technology discussed and demonstrated in this work has several advantages over previous methods of improving the performance of MEMS rotary micromotors. By comparison with any pinned or flanged motor design, or the wobble motor design, the liquid bearing technology removes all solid-solid contact and thus eliminates that significant source of friction, wear, and failure. The liquid bearing uses surface tension to replace the alignment functions of the solid-solid interfaces. Compared with hydrodynamic bearings, which use an oil film pressurized by herringbone grooves in the rotor and stator rotating at high rates of speed, liquid bearing technology operates in a much lower rotation-rate regime and can maintain static and moderate-speed alignment. Hydrostatic fluid bearings, which operate with an externally pressurized fluid, and levitation bearings which operate with an air gap created by electrostatic or magnetic fields have the disadvantage of requiring an external source of energy to provide positional alignment. Liquid bearings, conversely, are a passive positioning technology: all energy inputs in the system are used to rotate the motor. Finally, the previously studied micromotors that utilized liquid droplets were driven by electrowetting, and were limited in their maximum rotation rates. Liquid bearing technology permits use of the many driving mechanisms developed in MEMS, allowing an improved level of flexibility. Additionally, the positioning tolerances of liquid bearing technology are anticipated to greatly improve on other liquid droplet based motors.

2. Liquid Bearing Supported Rotary Motor: Design

2.1 Droplet Containment via Surface Patterning

In the liquid bearing motor, droplet containment is accomplished by patterning hydrophobic and hydrophilic regions on the rotor and stator, as shown in Fig. 21. The bearing fluids tend to stay in the hydrophilic regions and tend to stay off the hydrophobic regions as much as possible. The position of the droplets and their interactions with the rotor and stator coatings provide restoring forces.

A free rotor has six degrees of freedom (x,y,z translation, two out-of-plane rotations, and one in-plane rotation). To appropriately position the micromotor rotor, the liquid bearing must constrain the three translations and two out-of-plane rotations in a manner than permits low-friction in-plane rotation. The bearing constrains the non-desirable degrees of freedom through microscale fluid forces derived from surface tension effects.

2.2 Fluid Forces at Microscale

2.2.1   Surface Tension

Surface tension forces arise at the interface between multiple fluids and/or solid surfaces. In the case of liquid bearing technology, the interface is where the liquid, air, and rotor or stator surfaces meet, as shown in Fig. 4. For this derivation, the two fluids are considered a liquid, denoted by subscript l, and vapor, denoted by subscript v, with the solid surface denoted by subscript s. The surface tension for the liquid-solid interface is denoted γ_{ls}, for the liquid-vapor interface it is γ_{lv}, and for the solid-vapor interface, it is γ_{sv}. The tensions are a property of the fluid, the vapor, and the solid surface energy.

At the interface, a measurable property called the contact angle, θ, is defined as the angle between the fluid-vapor interface relative to the fluid-solid interface. The contact angle value depends on the surface tensions, γ_{ls}, γ_{lv}, and γ_{sv}. At equilibrium, the surface tensions must balance.
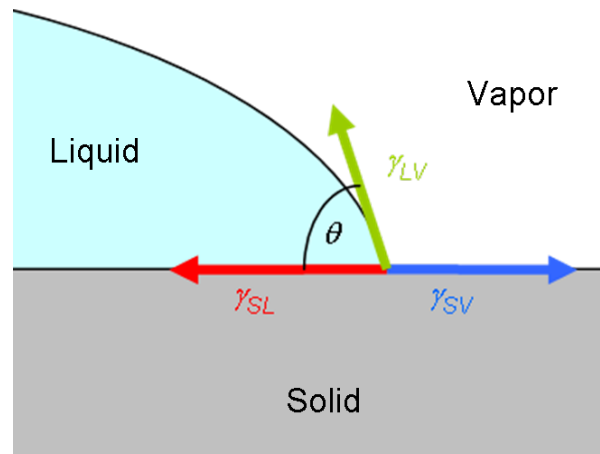

Fig. 4. Droplet interface schematic showing surface tensions along the solid-liquid interface, solid-vapor interface, and liquid-vapor interface.

Balancing the tensions in the direction parallel to the solid surface gives γ_{ls} - γ_{sv} = $\gamma_{la}\cos\theta$. The total force produced by surface tension (which is a force per unit length) is proportional to the surface tension, so the force balance equation can also be written F_{ls} – F_{sv} = $F_{lv}\cos\theta$. The force that arises parallel to the solid surface is what drives capillary action seen for fluids in small diameter tubes.

In the direction perpendicular to the solid surface, the tension force acting on the solid taken along the entire contact line of the interface, for a circular droplet with radius R, the force is given by:

$$F_T = 2\pi R \gamma_{lv} \sin\theta$$

(1)

2.2.2 Laplace Pressure

For a fluid droplet with no solid interface, surface tension will cause the droplet to form a spherical shape. The surface tension force induces an internal pressure, known as Laplace pressure, in the droplet to balance the tension.

Laplace pressure is the difference between pressures internal and external to a droplet, and is derived from the Young-Laplace equation describing capillary pressure difference for a two fluid interface. The Laplace pressure is described [40] by Equation (2). The left side of the equation, Δp, is the Laplace pressure difference, γ_{lv} is the surface tension at the vapor-liquid interface, the major droplet radius, R_1, and the minor droplet radius, R_2.

$$\Delta p = \gamma_{lv}\left(\frac{1}{R_1} + \frac{1}{R_2}\right)$$

(2)

For a droplet that doesn't contact a solid surface, assumed to be spherical so $R_1 = R_2$, the Laplace pressure as a function of radius is displayed in Table 2. The surface tension, γ_{lv}, is assumed to be $72 \cdot 10^{-3}$ N/m, the value for water at 25°C. Notice that as radius decreases, the internal pressure required to balance the surface tension force increases substantially, so a droplet with 100 μm radius has a Laplace pressure 100x that of a 10 mm droplet.

Table 2: Comparison of Laplace pressure as a function of droplet radius.

Radius	10mm	100μm	1μm	10nm
Δp [Pa]	1.440E+01	1.440E+03	1.440E+05	1.440E+07
Δp [atm]	0.00014	0.014	1.421	142.117

For a droplet between parallel plates, the Laplace force is based on major and minor radii. The major radius is generally the radius of the droplet, approximately equal to the contact line radius between the droplet and the parallel plates. The minor radius is generally the meniscus curvature of the droplet between the plates. A force differential occurs on the plates acting over the interface area of droplet, presumed to be circular with radius R, is shown schematically in Fig. 5 and given by Equation (3).

$$F_L = \pi R^2 \Delta p = \gamma_{lv}\left(\frac{1}{R_1} + \frac{1}{R_2}\right)\pi R^2 \tag{3}$$
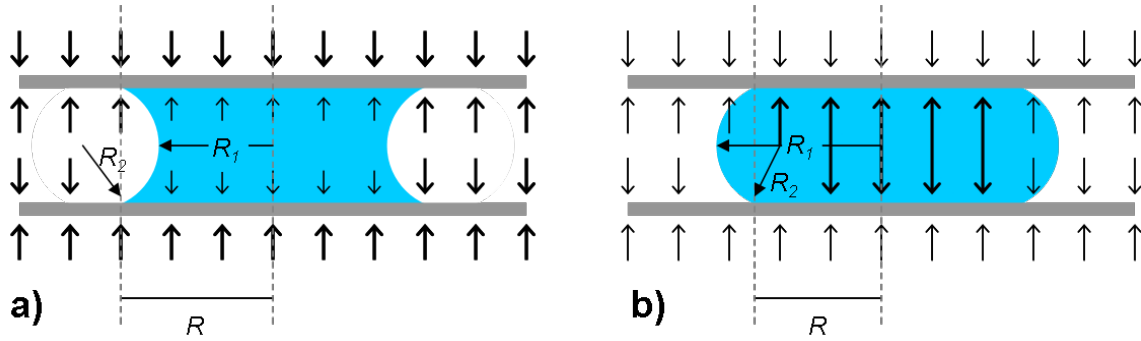
Fig. 5. The arrows perpendicular to the plates indicate the magnitude of pressure incident on the plate surface. a) Diagram of the pressure forces acting on parallel plates constraining a liquid droplet in tension. In this case, R_2, the minor radius of the droplet, is negative because the meniscus is concave. The resulting Δp, and therefore F_L is negative, so the droplet pulls the parallel plates together. b) Diagram of a droplet in compression. R_2 is positive in this case because the meniscus is convex, so the resulting Δp, and therefore F_L is positive, pushing the plates apart

2.3 Restoring Force models

Two surface tension based droplet forces are diagramed in Fig. 6. Based on Equations (1) and (3), an analytical model of compressive restoring force, F_{normal}, for a droplet in compression and tension between two parallel plates is developed [41, 42] for surface energy γ_{LV}, a configuration with bearing height, h, droplet radius, R, and contact angle θ. Equation (4) simplifies to the first terms in F_{normal} derived from Equation (3) due to the geometry of the droplet between parallel plates that is under consideration; when the droplet thickness is small compared to it's diameter, the minor radius dominates the Laplace force term and can be approximated by $1/R_2 = \cos\theta/h$.

$$F_{normal} = \frac{2\pi R^2 \gamma_{LV}}{h}\cos\theta_c + 2\pi R \gamma_{LV}\sin\theta_c \tag{4}$$

An analytical model [37, 43] of shear restoring force, F_{shear}, for a droplet in shear between two parallel plates is given in Equation (5) for surface energy γ_{LV}, a configuration with droplet radius, R, and contact angles θ_L and θ_R on the left and right sides, respectively:
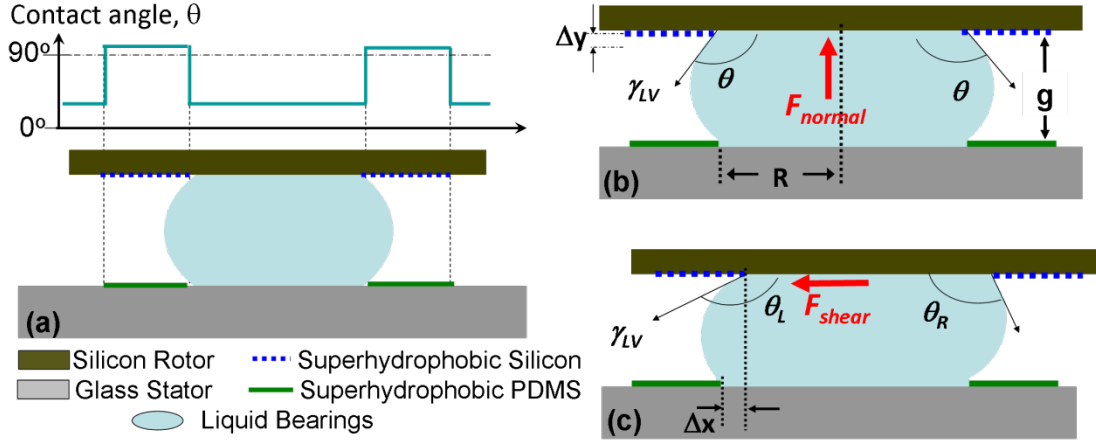
$$F_{shear} = \sqrt{2}R\gamma_{LV}(\theta_R - \theta_L) \tag{5}$$

Fig. 6. Schematic representations of a) the patterned regions whose surface energy defines the liquid bearing retention area, b) & c) restoring forces F_{normal} and F_{shear} induced in a droplet between parallel plates during loading, respectively.

2.4 Contact Angle vs. Surface Treatment

Hydrophobic surface coatings have been used in many MEMS applications, for example, as an anti-stiction coating [44, 45], drag reduction in microfluidics [46, 47], critical surface coatings for droplet-based microfluidics [30], biosensing applications [32], and in optical displays and lenses. Hydrophobic surfaces can be constructed using low surface energy material coatings which can be spun-on, CVD deposited or self-assembled onto the substrate. The hydrophobicity of a surface can also be improved by increasing surface area through increasing surface roughness. Microstructures on the surface form cavities or pockets in which air can get trapped, creating a composite solid-air-liquid interface which increases contact angle compared to a smooth interface with contact angle, θ_o. The performance of the liquid bearing micromotor may be improved by improving surface hydrophobicity of the micromotor patterned hydrophobic layers.
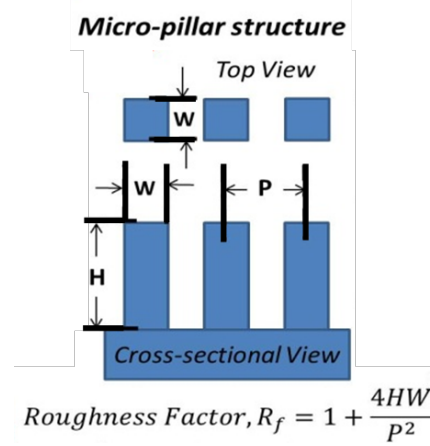
Micro-pillar structure

Roughness Factor, $R_f = 1 + \dfrac{4HW}{P^2}$

Fig. 7. Micro-pillar dimensions, W, H, and P, and roughness factor, R_f, calculation used for Cassie-Baxter and Wenzel contact angle models.

Two critical requirements to create a superhydrophobic surface ($150^{\circ} <$ contact angle, $\theta_c < 180^{\circ}$) are the surface roughness and the surface chemistry/energy. Cassie-Baxter and Wenzel models predict the contact angle for square micropillars, as depicted in Fig. 7. Roughness factor, R_f, is defined as the ratio of solid-liquid area to its projection on a flat plane, and can be expressed as:

$$R_f = 1 + \frac{4WH}{P^2} \tag{6}$$

where W is the width, H is the height and P, the pitch between the pillars.

The Wenzel model assumes the droplet is in total contact with the rough surface with no air pockets, the contact angle, θ_c is given as [48]:

$$\cos\theta_c = R_f \cos\theta_o \tag{7}$$

The Cassie-Baxter model modifies the Wenzel model by assuming air pockets in the rough surface, and considers the composite interfaces involving both liquid-air and solid-air interfaces by including the contribution from the fractional area of the wetted surfaces, f_{SL} as well as the fractional area with air pockets, $1\text{-}f_{SL}$. [49]

$$\cos\theta_c = R_f f_{SL} \cos\theta_o - 1 + f_{SL} \tag{8}$$

The fractional area of the solid liquid interface, f_{SL}, for the square pillars can be described as:

$$f_{SL} = \frac{W^2}{P^2} \tag{9}$$

2.5 Surface Treatments

2.5.1   Hydrophobic Glass Teflon (Cytop)

The bearing geometry is defined by patterning the surfaces of the rotor and stator with a 2 µm thick hydrophobic amorphous fluorocarbon layer (Cytop, Asahi Glass Co.). The contact angles of water and ethylene glycol on the Cytop surface are ~99 and ~94 degrees respectively. The relatively high surface energy of glass and silicon allows the bearing liquid to wet the exposed surfaces, while the hydrophobic Cytop layer pins the bearing edges to a fixed location.

2.5.2   Superhydrophobic Cytop Coated Microstructures

Many studies demonstrate fabrication techniques to produce roughness on silicon substrates [50-52]. In this work, the focus is creating microstructure arrays compatible with the standard microfabrication process steps for liquid bearing micromotor, where a more resilient superhydrophobic (SHP) coating is required to withstand the subsequent processing steps. The fabrication process for the superhydrophobically patterned silicon rotor is detailed in Fig. 8. Single crystal silicon is patterned using standard photolithography techniques. A deep reactive ion etcher (DRIE, Alcatel 601E) etches the micro-structures to a height of ~10 µm. An acetone rinse and oxygen plasma cleaning step is carried out to remove all remaining photoresist , before the final spin coating step (~1000 rpm) to coat an uniform conformal layer of fluoropolymer, Cytop (Asahi Glass) atop the microstructures.

The rotor is a 10 mm diameter disk etched from a 300 µm thick silicon wafer. Photoresist and DRIE etch form frontside features for permanent magnet alignment, as well as backside features. The backside features are subsequently covered with Cytop to create the superhydrophobic droplet confinement regions. Finally, the disks are patterned and released by DRIE through-wafer etch.

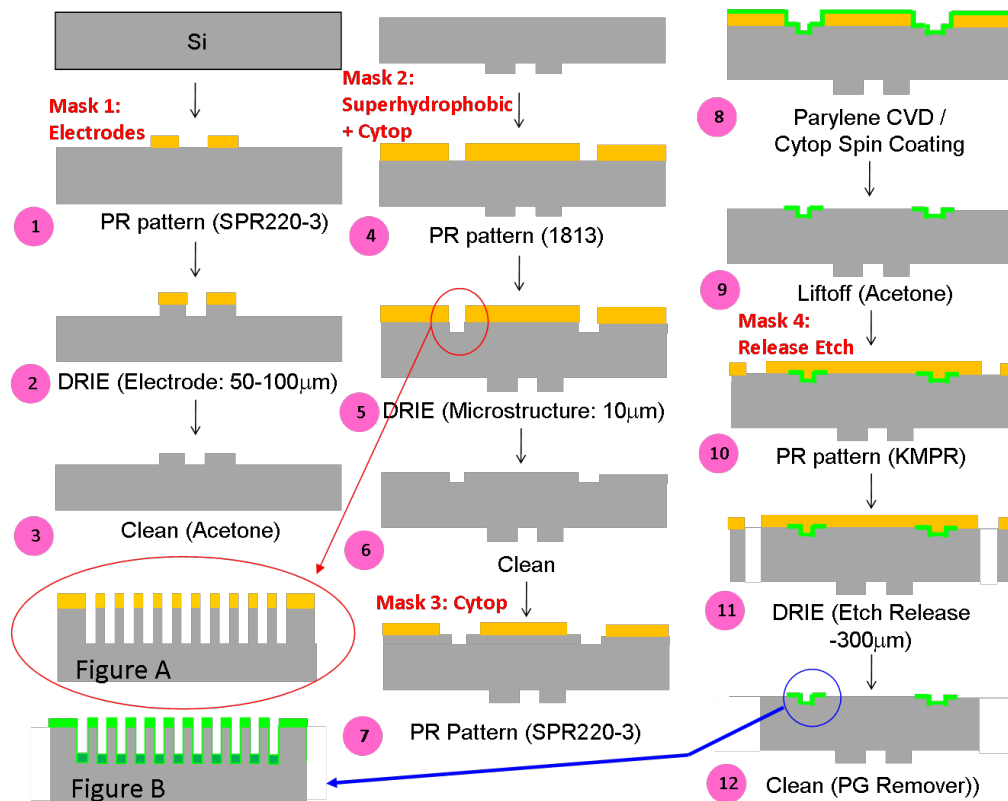**Superhydrophobic Rotor Process Flow**

Fig. 8. Fabrication process flow for superhydrophobic rotor.

Fig. 9 shows Scanning Electron Microscope (SEM) images of the superhydrophobic features on the rotor at two stages in the processing. Fig. 9 a) is an image of the micropillars after the DRIE etch step (5 in Fig. 8), and clearly shows the classic scalloped sidewalls produced in the DRIE process. Fig. 9 b) shows the micropillars after coating with Cytop (step 12 in Fig. 8).
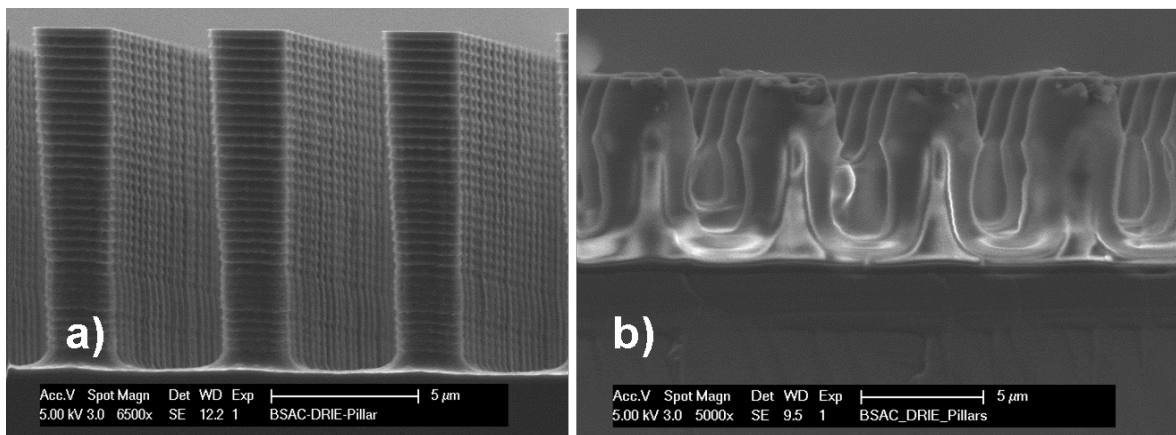

Fig. 9. Micropillars etched in Si a) before and b) after coating with Cytop flouropolymer to create superhydrophobic surface.

2.5.3   Superhydrophobic Laser Etched PDMS

Two stator designs were tested based on the fabrication method described in [53]. The stators consist of a glass slide spin- or cast-coated with 50 μm thick PDMS pre-polymer layer (10:1 mix of PDMS precursor with curing agent, Sylgard 184) that is laser-etched (at 11 mm/s scan speed and 1.1 W power, Universal Laser), as shown in Fig. 10, to create a nano-featured SHP surface. Laser ablation of the PDMS surface creates hydrophilic regions for droplet retention. The contact angle of the surface depends on the parameters of the laser etching process.
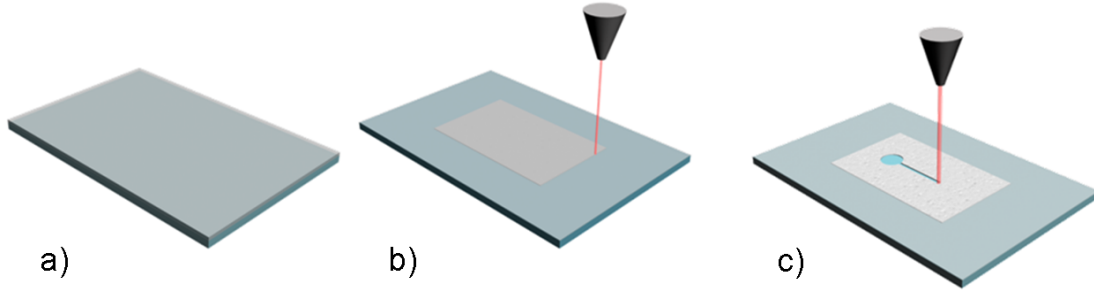
Fig. 10. PDMS SHP coating fabrication. a) Spin or cast-coat PDMS pre-polymer on glass, b) laser-etch to create nano-structured SHP coating, and c) laser ablation of PDMS to define hydrophilic droplet retention regions.

The stator superhydrophobic surface coatings were fabricated by the group of Prof. Tingrui Pan in the UC Davis Biomedical Engineering Department. The PDMS layer is laser-etched to create the superhydrophobic ring, shown in Fig. 11. The center dark area is the hydrophilic region that the central droplet aligns to. The contact angle of the surface depends on the laser etch pattern.
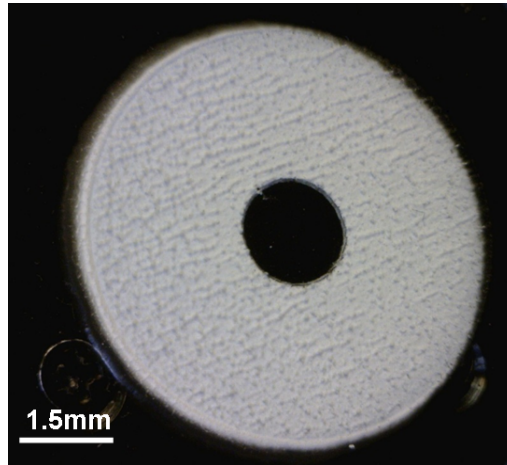

Fig. 11. Microscope image of the laser-etched PDMS surface showing the central hydrophilic region for bearing registration and the outer, white superhydrophobic surface.

To demonstrate the effect of contact angle on bearing performance, two surfaces were tested: one formed with optimized etch parameters and a second formed with an underpowered etch. Scanning Electron Microscope (SEM) images of the optimally etched PDMS coating are shown in Fig. 12 at varying magnification levels to demonstrate the multiple length-scale roughness features. The underpowered etch is shown in Fig. 13. Fig. 14 directly compares the nanoscale features of the two etched surfaces. There is a significant difference in the nanoscale roughness of the two coatings, the optimally etched coating shows a rougher surface with features on the order of a few hundred nanometers, whereas the underpowered etch coating has micron length features.
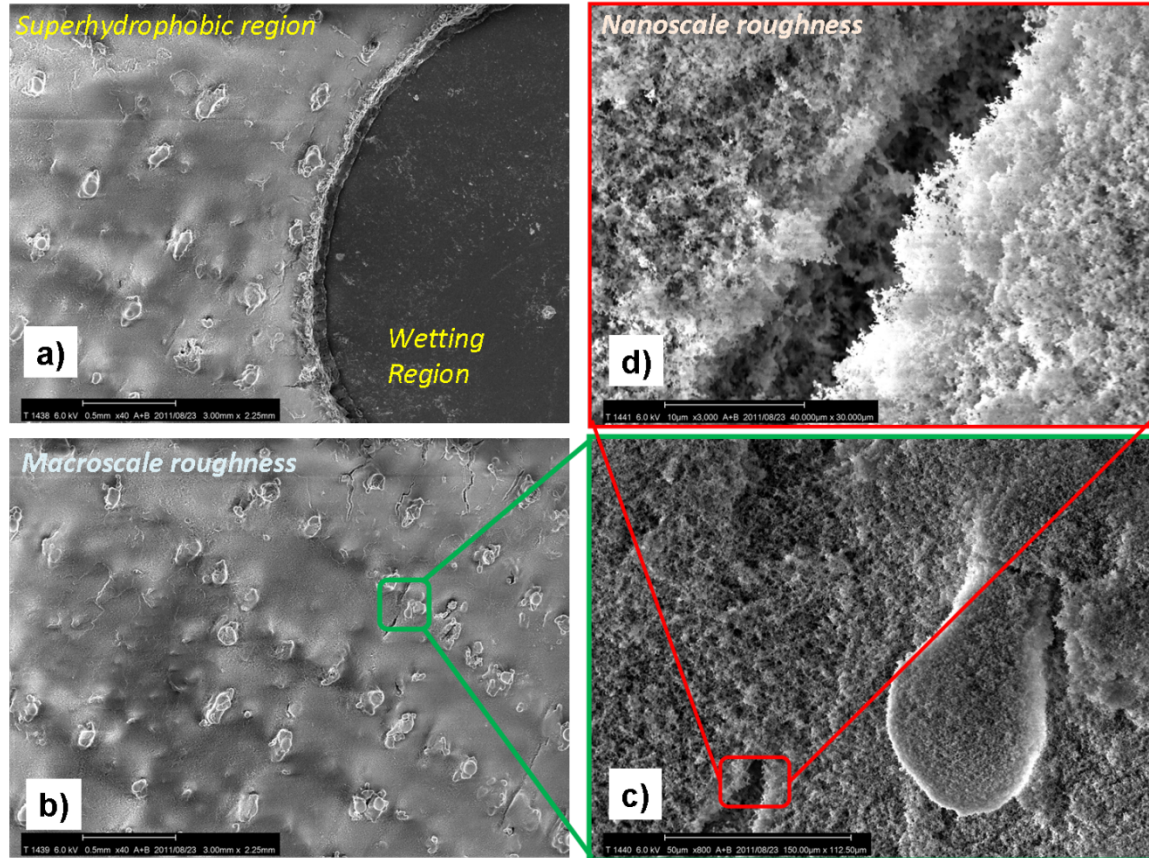
Fig. 12. SEM image of optimally etched stator superhydrophobic surface: a) is the macroscale image showing the difference between superhydrophobic and wetting regions: b), c) and d) are various magnification level images of the superhydrophobic surface. The scale bars in the insets are 500 μm, 50 μm, and 10 μm.
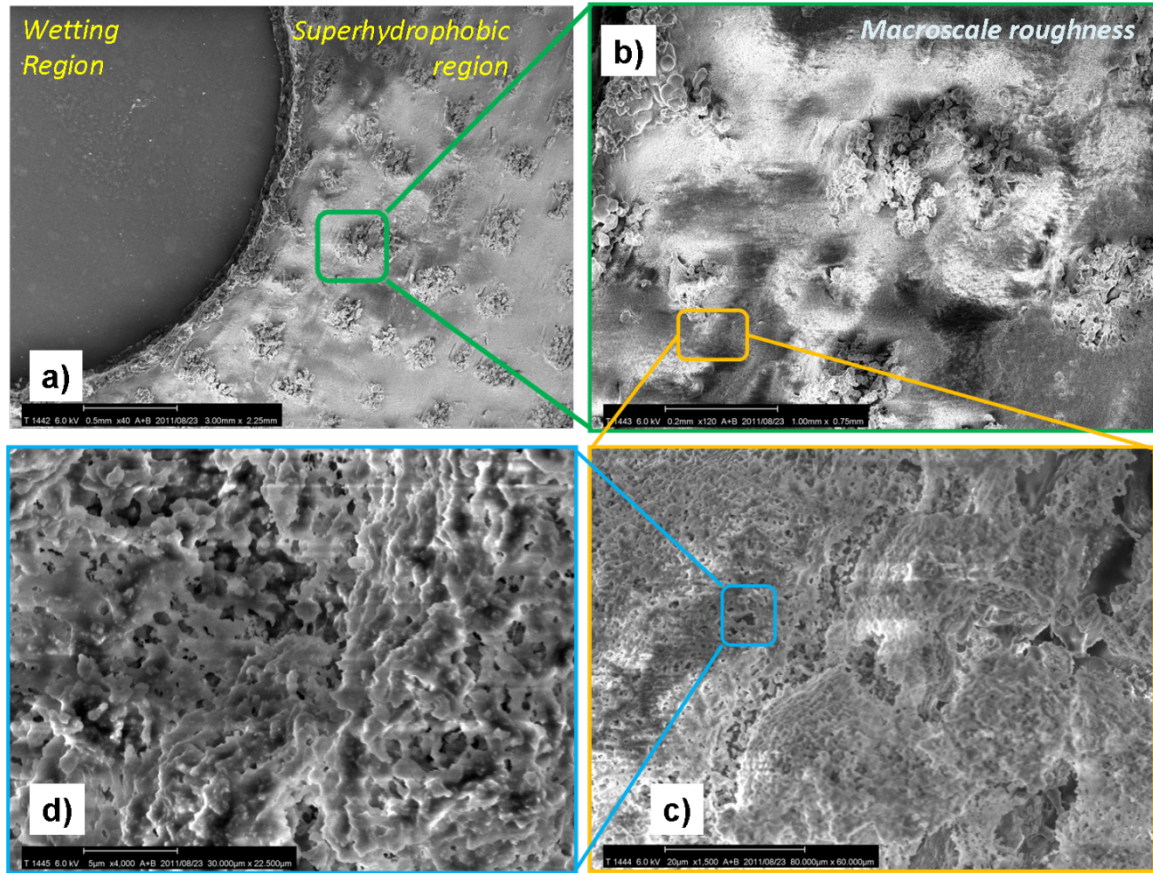
Fig. 13. SEM image of underpowered etch stator superhydrophobic surface: a) is the macroscale image showing the difference between superhydrophobic and wetting regions: b), c) and d) are various magnification level images of the superhydrophobic surface. The scale bars in the insets are 200 μm, 20 μm, and 5 μm.
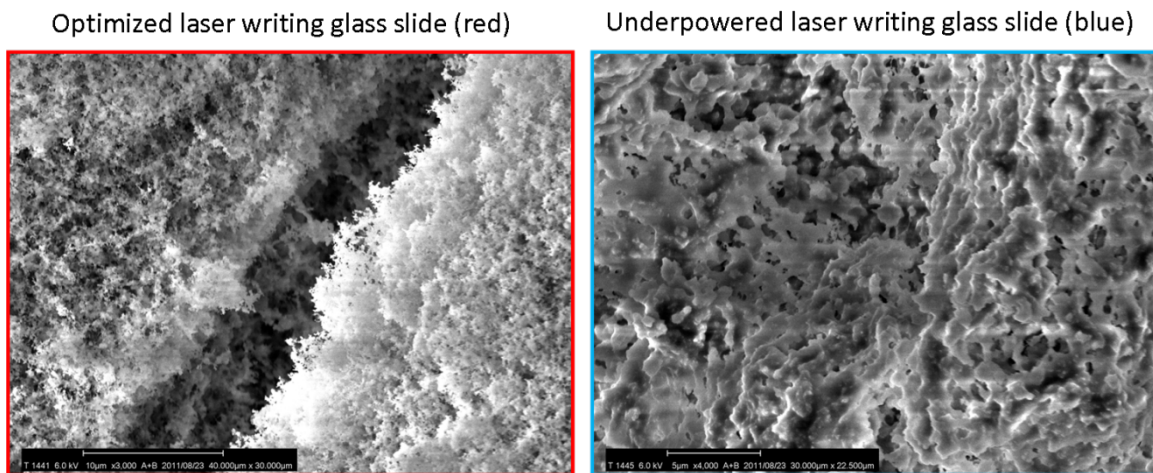

Fig. 14. SEM images directly comparing the nanoscale roughness of the optimized etch coating on the left and underpowered etch coating on the right. The optimized etch coating shows significantly more small-scale features than the underpowered etch case, leading to improved superhydrophobic performance.
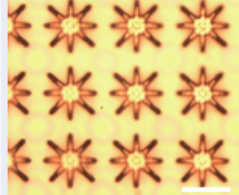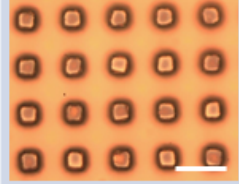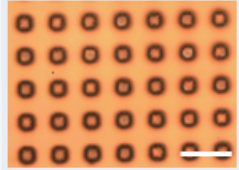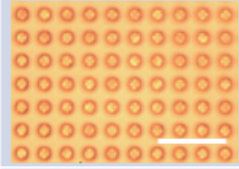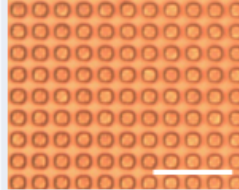
2.6 Surface Treatment Performance
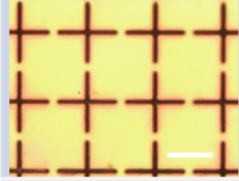
2.6.1 Patterned Silicon Study

An experimental study of patterned silicon surfaces with various heights, H, widths, W, and pitch, P, as shown in Table 3, is conducted to investigate the dependence of the contact angle, θ_c, on the geometrical parameters, and shows smaller structures with higher aspect ratio results in an increased superhydrophobicity. All of the micro-structured geometries show better performance than Cytop coated Si with no micro-features which has a static contact angle of ~98°.

Scanning Electron Microscopy (SEM) is used to image the cross section profile of the structures in Table 3 to determine their dimensions. The experimental data is plotted against the Wenzel and Cassie-Baxter model in Fig. 15. The measured contact angles increased with the roughness factor, following the trend of both models, but lies between the predicted contact angles from the two models. The deviation from the predicted Cassie-Baxter model for a composite interface can be attributed to the surface defects resulting from the spin-coating of the Cytop layer. SEM image of the micropillars after Cytop coating, in Fig. 9 b), shows prominent bumps and grooves at the sidewalls of the pillars. These bumps/grooves have been shown to create stable/unstable equilibrium points at the liquid-air interface, causing variations in contact angles [54].

Much higher contact angles have been reported by generating nanoscale roughness on silicon substrate [55] or using a two-tier roughness profile [56]. These techniques pose tremendous challenges when incorporated with other processing steps to develop a functional device with high yield. Therefore the superhydrophobic surface for our devices is confined to micro-structures dimensions with a width and pitch of 2-3μm and aspect ratios ~4. The best performing surface from the study was fabrication on the rotor.

Table 3: Summary of various geometries used to create micro-structure on silicon surface to increase surface roughness and hydrophobicity. First column on the left shows the optical micrographs of the etched microstructures on silicon: the white scale bar for all the figures indicated 25μm. The second column lists the geometrical parameters, while the last column shows the measured average contact angles taken at three different locations on the die.

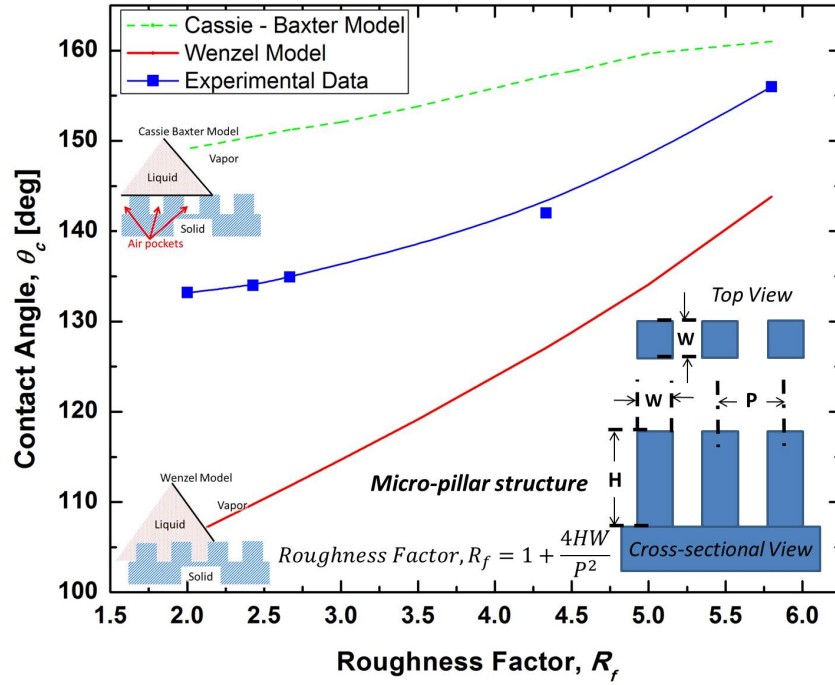| Geometry	Dimension	$\theta_{c,water}$
	Cross Width = 30μm Pitch = 36μm Aspect Ratio = 0.5	105.1
	Star Width = 22μm Pitch = 30μm Aspect Ratio = 0.5	128.9
	Square Width = 10μm Pitch = 20μm Aspect Ratio = 1.3	133.2
	Square Width = 6μm Pitch = 12μm Aspect Ratio = 2	134.9
	Square Width = 3μm Pitch = 6μm Aspect Ratio = 4	142.4
	Square Width = 3μm Pitch = 5μm Aspect Ratio = 4	156.1

Fig. 15. Plot of the predicted and measured contact angle of water on silicon wafer patterned with micropillars. The experimental results (▪) follows the trend of both the Cassie-Baxter (- -) model and Wenzel (−) model, where increasing roughness factor results in an increase in contact angle. Inset: illustrates the cross-sectional and top view of the micropillar and the geometrical parameters used for roughness factor calculation.

2.6.2   Contact Angle Measurements

The contact angle of the liquid droplet with the superhydrophobically-patterned surface indicates how much restoring force will be provided to correct for positional and angular misalignments between the rotor and stator, as discussed in section 2.2. Two contact angle measurements are relevant to the restoring force; a static contact angle measurement for a droplet at rest on a surface normal to the direction of gravity, and the advancing/receding contact angle measurement, measured on a surface that is tilted relative to gravity normal immediately prior to droplet sliding.

Measurements of water droplet contact angle on the micro-patterned silicon rotor at rest and immediately prior to sliding are shown in Fig. 16 a) and b) respectively. The static contact angle measurement is 17.2^o and the advancing/receding contact angles are $14.0^o/17.5^o$.

Fig. 17 shows the advancing and receding contact angle measurements on the laser-etched PDMS coated glass stator for the a) optimized and b) underpowered etch coatings. The optimized surface has a difference between θ_{adv} and θ_{rec} of 10°, while the underpowered etched surface had a contact angle difference of 44°.
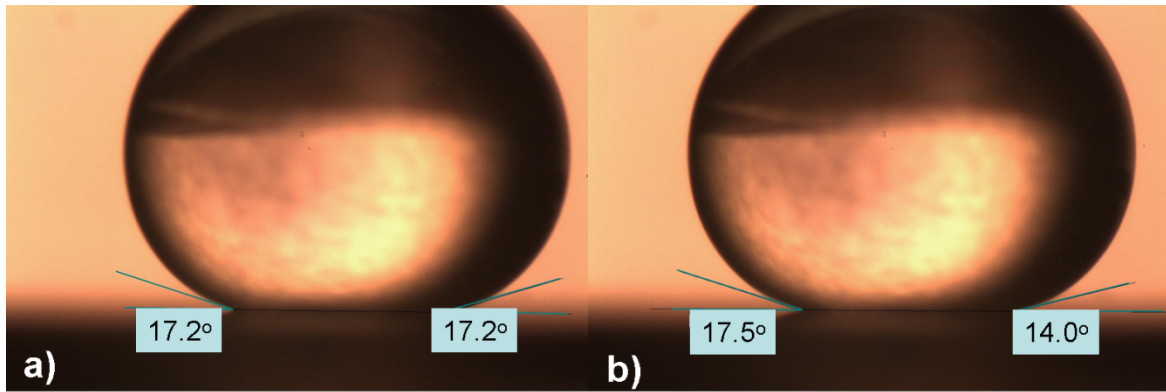
Fig. 16. Water droplets on the superhydrophobic Cytop on silicon pillar coating used on the rotor in a) the static condition and b) immediately prior to sliding to the right. The difference between advancing and receding contact angles in b) is 3.5°.
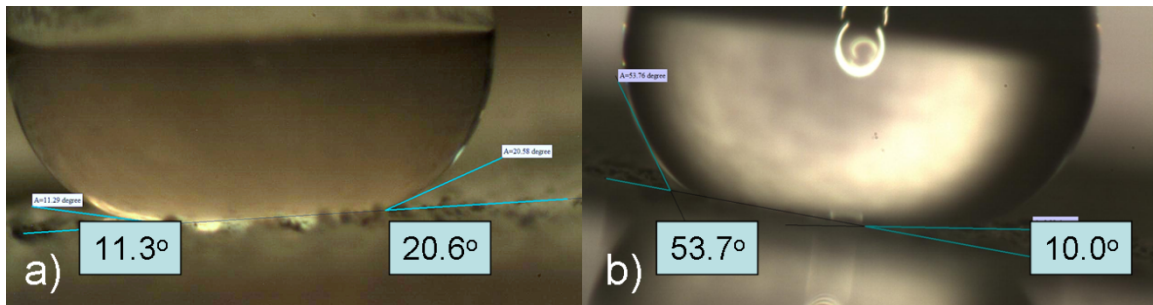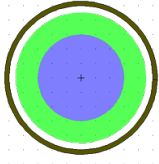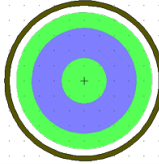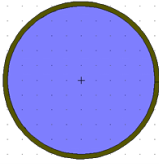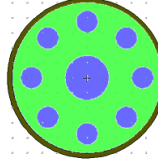

Fig. 17. Advancing and receding contact angle measurements immediately before droplet sliding for a) optimally etched PMDS are 10° and 20° respectively, and for b) underpowered etch PDMS coatings are 10° and 54° respectively.

2.7 Design

Four device designs have been developed and tested through the process of creating a liquid bearing for rotary micromotor support. The bearings are summarized in Table 4.

Table 4: Summary of liquid bearing designs discussed. The disk, ring, and satellite designs all use hydrophobic surface patterning for liquid droplet positioning and retention. The full bearing design uses a walled stator to maintain the fluid.

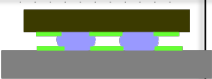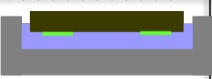| Bearing Design	Disk Bearing	Ring Bearing	Full Bearing	Satellite Bearing
Top View of Bearing ■ Liquid ■ Cytop				
X-Section of Bearing	rotor / stator			
Rotor Radius [mm]	5	5	5	5
Bearing Radius [mm]	3	Inner = 1.5, Outer = 3.5	5	Central = 2.5 Satellite =0.5

All of the designs that were tested were created on circular rotors with 5 mm radius and 300 μm thickness. The disk bearing has a single droplet constrained at the center of the rotor and stator by Cytop patterning. The disk bearing was fabricated with hydrophobic surface patterns defining the fluid retention region that varied between 2.5 and 4 mm in radius, with selection of a 3 mm radius bearing for testing.

The ring bearing is similar in design and construction to the disk bearing, but the fluid layer is constrained to a ring or toroidal shape between the rotor and stator. The ring bearing was fabricated with various hydrophobic surface patterns that varied the ring thickness between 1 and 2 mm, with selection of a design with 1.5 mm inner radius and 3.5 mm outer radius for use in testing.

The full bearing design features a bearing that covers the entire bottom surface of the rotor and is captured in a well in the stator, in essence creating a floating rotor. The rotors used in testing were identical to the disk bearing rotors. The stator was fabricated with a 5.3 mm radius to allow clearance for the spinning rotor. No hydrophobic coating was applied to the stator.

The final design, the satellite bearing, has a large droplet in the center of the rotor and stator that is constrained in the same manner as the disk bearing, but also consists of several satellite droplets that are constrained on the rotor by hydrophobic coating but permitted to slide freely over the hydrophobic coating on the stator layer. The central droplet hydrophobic surface patterns were fabricated in various sizes from 1 mm to 3 mm radius with selection of a 2.5 mm radius droplet for testing. The satellite droplets varied between 0.5 mm and 1.5 mm radius with 0.5 mm being selected for testing.

The various fabricated bearing dimensions were used to experimentally determine good characteristics in terms of ease of use, performance, and durability. Very narrow

hydrophobic surface patterns were unable to contain the droplets during assembly and some testing configurations. As a result, the bearing geometries used in tests, as indicated previously, had hydrophobic containment regions minimally 1 mm wide, either between a droplet and the rotary motor edge, or between adjacent droplets in the case of the satellite bearing design.

2.7.1 Assembly

Deposition of the liquid droplets onto the rotor is done manually by micro-pipette. The rotor is then aligned and placed onto the stator by a vacuum pick-and-place tool attached to a six-axis stage with micrometer positioning capability. The rotor, with eight satellite droplets and a single anchor droplet, is suspended over the stator surface by a vacuum tool head, shown in Fig. 18. The PDMS SHP coating is visible on the stator surface with the smooth, hydrophilic region in the center to align the anchor droplet.
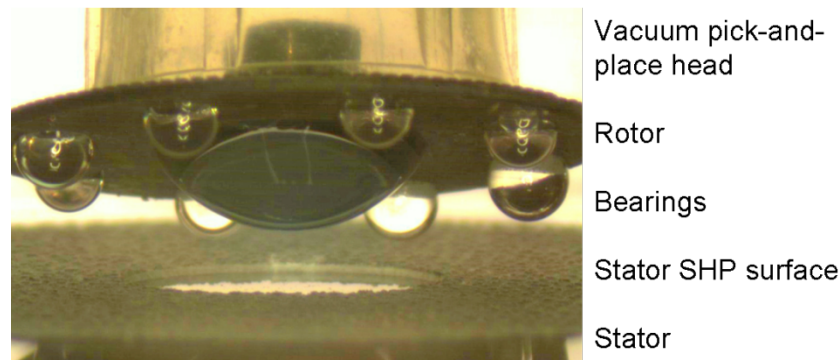

Fig. 18. Image of the rotor, stator, and liquid bearings during assembly process. Clearly visible are the 8 satellite bearings and single central bearing, the superhydrophobic stator coating with patterned anchor location for central bearing, and vacuum pick-and-place tool head.

2.7.2 Test bed development

Various methods of actuating the rotary micromotor were considered at the outset of designing the liquid bearing project. Electrostatic drive has been a mainstay of rotary micromotor designs since their inception as center pinned, flanged, and wobble motors discussed in the introduction. Electrostatic motors function by variable pole area overlap, and typically work well for gap sizes on the order of 1-20 μm. The positioning capability and lateral stiffness of the liquid bearing make tolerances of that level challenging. Both side drive and bottom drive electrostatic motors were fabricated early in the design and test phases of the liquid bearing, but due to the immature state of the liquid bearing at the time, they did not function well.

Alternative drive mechanisms were considered, but magnetic drive was selected for testing. Magnetic drive is well suited to the test environment for a number of reasons. The test stand fabrication is done at the macroscopic level and is tolerant to misalignments on the order of 1-10 mm. Providing the drive electronics and control for the magnetic field is also straight-forward. Control signals are created in Labview which vary the signal amplitude and phase going to each Helmholtz coil pair. Amplifiers take

the Labview output via DAQ cards and create high currents that are used to drive the magnetic field.

For a Helmholtz coil pair, the field, B, at the center of the coils can be described by Equation (10), where μ_o is magnetic permittivity in air (assumed equivalent to the permittivity of vacuum), n is the number of turns in the coil, I is the coil current, R is the radius of the coil, and x is the distance from the center to each coil.

$$B = \frac{\mu_o nI}{\left(R^2 + x^2\right)^{3/2}} R^2 \tag{10}$$

For the setup that was used in characterizing the liquid bearing, there were two sets of orthogonal coils, with the inner pair positioned such that x was equal to R, and the outer coils positioned as closely as possible outside the inner pair. The geometry of the system gave the values of field per amp of $B_{inner} = 4.5e^{-3}$ [T/A] and $B_{outer} = 2.5e^{-3}$ [T/A]. The control values from Labview were set such that the field produced by each coil pair was equal. Assuming superposition of the magnetic fields, and by applying sinusoidal fields 90° different in phase, a rotating field is created of uniform intensity and rotating at the frequency of the sinusoids.

2.8 Measurement devices

Measurements of the positioning and geometry of the liquid bearings were done using a suite of laboratory instruments. A Polytec Laser Doppler Vibrometer (LDV) was used in determining the positioning of the micromotor in various tests. The LDV operates by measuring interference fringes between a reference and a laser reflected off the surface of the device under test (DUT).

Camera images taken through a microscope were used to measure bearing thickness and tilt of the rotor for several tests. An image of the rotor is shown in Fig. 19. Pixel size is calibrated so image data can be converted to physical units. The image profile is taken in two locations, one at the rotor center and another toward the edge. By measuring distance between the rotor and stator, the bearing thickness and tilt can be calculated. Intensity profile lines 1 and 2 are shown in Fig. 20 for 16 different drive configurations.
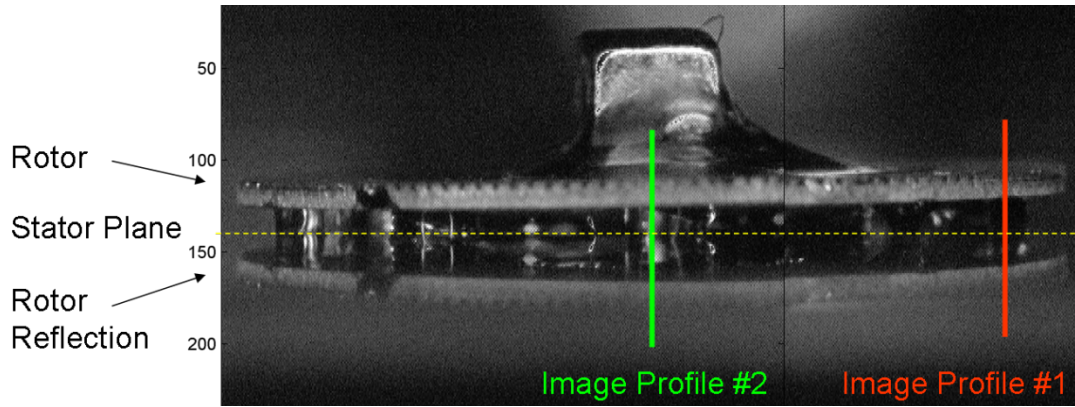
Fig. 19. Camera image of the rotor assembly taken through a microscope. The stator is a reflective surface in this test, so the camera image shows a reflection of the rotor across the stator plane. Image scale is in pixels, approximately 10 micrometers per pixel.

Fig. 20. Intensity profile of line #1 and #2 from Fig. 19 for several test configurations are cross-plotted. The number of pixels between the rotor and stator can be converted into physical units (10 μm/pixel) to calculate bearing thickness and tilt.

Fig. 21. Schematic representation of the wobble measurement technique. The PSD measures two-axis displacement of a laser beam reflected off the rotor surface, a distance L away, during rotation. The beam motion is twice the rotor motion.
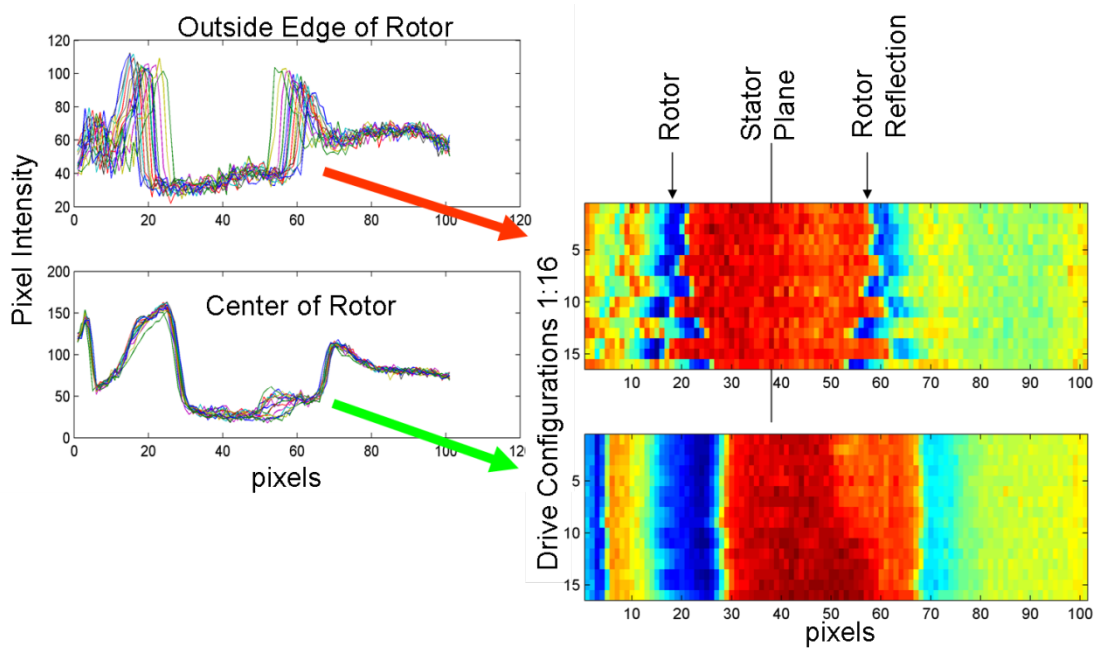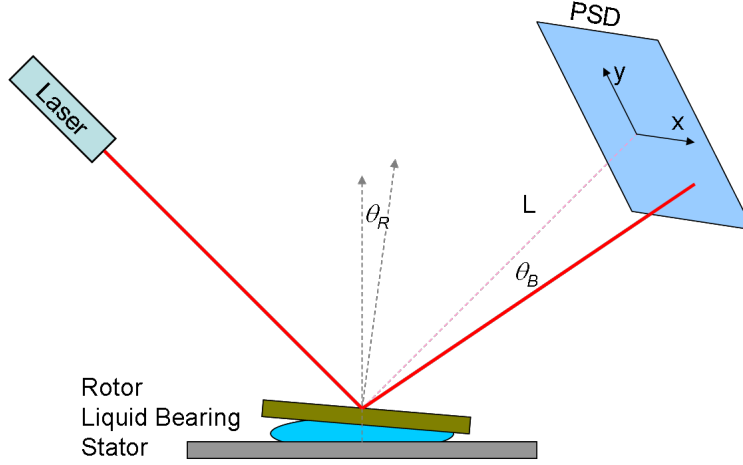
Laser based interrogation of rotor tilt done with a two-axis position sensing diode (PSD) for measurement of wobble as shown schematically in Fig. 21. The laser is reflected off the top surface of the rotor at 45° to the stator normal axis. The laser beam is incident on the PSD at approximately normal incidence. For a laser beam reflected off a moving surface, the beam angle change, $\Delta\theta_B$, is twice the angular change of the surface, $\Delta\theta_R$. The beam translates on the PSD by an amount equal to the distance between rotor and PSD, L, multiplied with the beam angle change. Equations (12) & (12) describe the rotor angle as a function of the system configuration and the PSD measurements.

$$\theta_{R,X} = \frac{1}{2}\theta_{B,X} \approx \frac{1}{2}\left(\frac{PSD_X}{L}\right) \tag{11}$$

$$\theta_{R,Y} = \frac{1}{2}\theta_{B,Y} \approx \frac{1}{2}\left(\frac{PSD_Y}{L}\right) \tag{12}$$

3. Liquid Bearing Supported Rotary Motor: Models & Experiments

3.1 Models & Simulations

3.1.1 Satellite Bearing Tip/Tilt Restoring Torque Model

The liquid bearing design using satellite droplets improves over the disk, ring, and full bearing designs presented in [14] by producing a restoring torque to correct tip and tilt of the rotor relative to the stator. The satellite droplet design utilizes eight small droplets near the rotor edge to produce the restoring torque and a single central droplet which maintains axial alignment between rotor and stator, as shown in Fig. 22(a).

Fig. 22c describes the tip/tilt restoring torque. For an induced tilt, the right-hand satellite droplet contact angle increases while the left-hand droplet contact angle decreases. Normal restoring force increases with contact angle as shown in Equation (4). The resultant torque described in Equation (13) is the sum of the normal force, $F_{i,normal}$, multiplied by the distance to the tilt axis, L_i, for each of the 8 satellite droplets:

$$\tau_{result} = \sum_{i=1}^{8} F_{i,normal} L_i \tag{13}$$
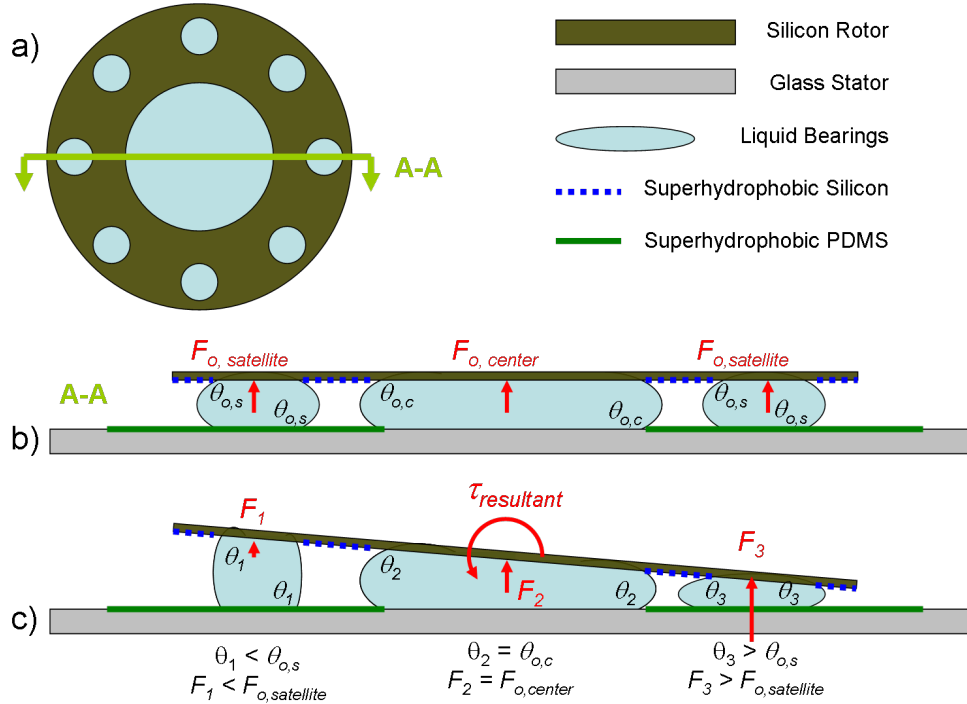

Fig. 22. a) Satellite bearing retention locations defined by superhydrophobic micropatterns, b) cross section A-A showing relationship of rotor, liquid bearings and stator, and c) mechanism for tip/tilt restoring torque given induced rotor tilt.

A simulation of restoring torque for tip/tilt was done in Surface Evolver [57], a numerical solver that models the total energy, from surface tension, gravity, and external forces, and evolves the surface shape until a minimum energy position is reached. Two models were created, one for the single droplet disk bearing design and a second model for the satellite bearing design. Fig. 23 shows the visual representation of the satellite bearing model, simplified to only having two satellite droplets at the maximum displacement locations.
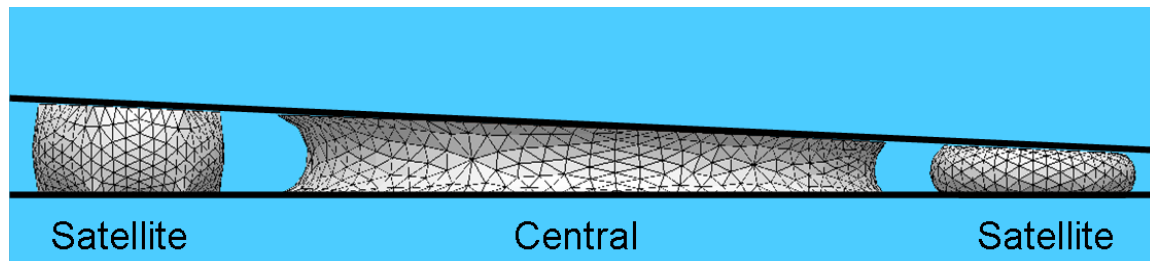

Fig. 23. Surface Evolver visual representation of the surface shapes during a minimum energy evolution for a simplified satellite bearing design. The satellite droplet on the left has a smaller contact angle than the satellite droplet on the right.

Several surface evolver test cases were evaluated; the volume of the droplets is held fixed but the tilt angle of the rotor relative to the stator is varied for each test case. Surface Evolver scripts are used to consistently define the surface mesh across the test cases; the program seeks the total minimum energy position for the mesh surface elements. A plot of the simulated total energy is plotted against bearing tilt angle in Fig. 24. The total energy value does not necessarily correspond to a real energy unit, the program is strictly numerical and no calibration test cases were run. The important characteristic of the simulation result is the trend of the energy as a function of tilt angle. The trend shows a decrease in energy with decreased tilt, and a minimum energy at zero degrees tilt.
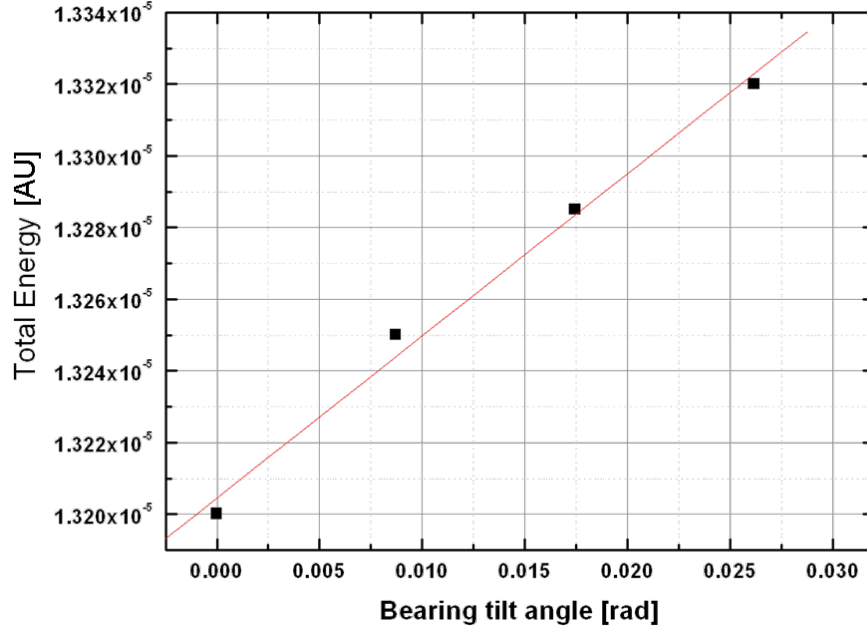
Fig. 24. Surface Evolver total energy calculation at minimum energy evolutions for fixed rotor tilt angles.

3.1.2 Disc and Ring Bearing Rotational Drag Torque Model

A liquid bearing with low viscosity, μ ($\mu_{H2O} = 1$ mPa·s, $\mu_{EG} = 16.1$ mPa·s), allows the rotor to operate in a low friction domain. The viscous friction characteristics of the liquid bearing are a function of fluid thickness and radius and are modeled by the viscous drag coefficient, b:

$$b = \frac{\mu \pi R^4}{2h} \tag{14}$$

Static friction properties of the bearing have a more complicated origin, depending on both the curvature of the bearing edge and roughness created by imperfections of the bearing boundary.

3.1.3 Satellite Bearing Rotational Drag and Startup Torque Models

Minimum startup torque for the satellite droplet bearing supported rotor is a function of the shear restoring force from Equation (5). The satellite droplets are pinned to the rotor by the patterned surface. Above the minimum torque input, the satellite droplets move across the surface of the superhydrophobic stator coating.

The contact angles θ_R and θ_L correspond to the advancing and receding contact angles (θ_{adv} and θ_{rec} respectively) specific to the stator surface treatment and liquid used in the bearing. The startup torque in Equation (15) is the sum of the shear restoring force, F_{shear}, times the distance from the satellite droplets to the axis of rotation:

$$\tau_{startup} = \sum_{i=1}^{8} F_{i,shear} L_{i,SB} \tag{15}$$

Maximum rotation rate as a function of input torque allows direct measurement of the drag coefficient for the liquid bearing. Equation (10) is a simply second order model of the rotor stator system, where I is the moment of inertia for the rotor, b_{drag} is the rotational drag coefficient, and k is the rotational stiffness of the liquid bearing. θ, ω, and α correspond to angular position, velocity, and acceleration respectively, and τ_{input} is the input torque. When the rotor is spinning, the liquid bearing provides no restoring force, so $k = 0$. At steady state rotation, angular acceleration, $\alpha = 0$. Thus, the Equation (16) simplifies to Equation (17).

$$\tau = I\alpha + b_{drag}\omega + k\theta \tag{16}$$

$$\tau_{SS} = b_{drag}\omega \tag{17}$$

3.1.4 Torque from Magnetic Drive

The mechanical performance of the liquid bearing micromotor was characterized using magnetic actuation to spin the rotor. Two orthogonal pairs of Helmholtz coils are driven with currents that are 90° out of phase, at matched amplitudes, to create a rotating magnetic field with uniform magnitude in the range of $B = 1$ mT. The frequency of the coil signal, Ω, determines the motor rotation rate while the field amplitude provides control over the applied torque.

Fig. 25 is a schematic of the Helmholtz coil pair's positions relative to the rotary micromotor and theory of operation. The inset at top right shows the orthogonal pairs of coils with inputs 90° out of phase. The schematic at bottom left shows the micromotor assembly with field lines from the Helmholtz coil pair interacting with the permanent magnet mounted on the rotor.

For applied magnetic field, B, and rotor magnetic moment, m, the torque on the rotor is described in Equation (18). Maximum torque is achieved when the angle, ϕ, between B and m is 90°, and is simply the product $max(\tau_{applied}) = Bm$.

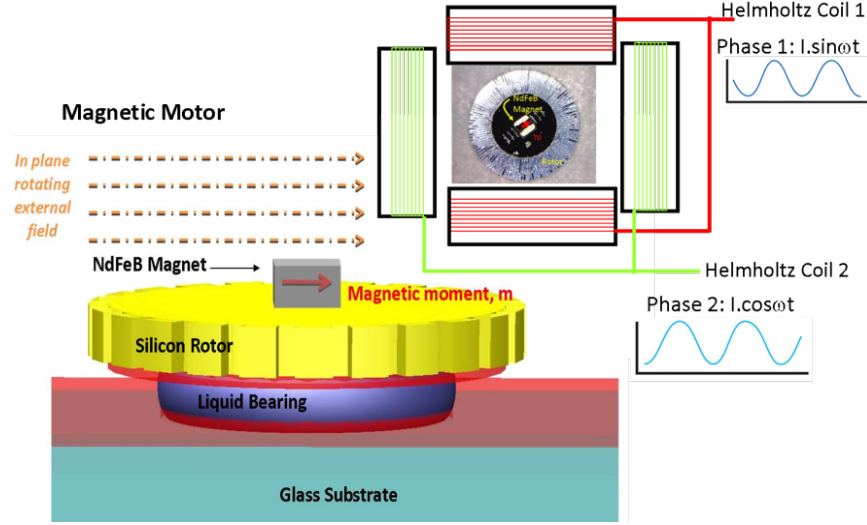$$\tau_{applied} = \bar{m} \times \bar{B} = |m||B|\sin\phi \tag{18}$$

Fig. 25. Schematic of the liquid bearing structure used to support a silicon rotor on a glass substrate. An NdFeB magnet mounted on the silicon rotor follows the rotating magnetic field generated by the two-axis Helmholtz coils.

3.2 Test and Characterization

3.2.1 Functional / Survival tests

3.2.1.1 Static Pull-off Force Measurements

As described by Equation (4), surface tension creates either adhesive or repulsive forces to: (1) prevent separation of rotor from stator or (2) support the rotor. In the case where the motor is inverted and gravity pulls the rotor away from the stator, as illustrated in Fig. 5a, a concave-shaped meniscus bridge forms between the hydrophilic part of the stator and rotor. Referring to Equation (3), the concave shape of the liquid interface ($\theta < 90^{\text{o}}$) results in negative Laplace pressure inside the bearing liquid. This negative pressure results in an intrinsic adhesive force between the stator and rotor and retains the rotor in place. On the other hand, when the motor is upright, the gravitational force compresses the bearing and the liquid interface assumes a convex shape. A convex meniscus interface angle ($\theta > 90^{\text{o}}$) creates a positive Laplace pressure and repulsive F_{normal}, as illustrated in Fig. 5b. The contact angle between the fluid and Cytop surface defines θ_{max} and thus $max(F_{normal})$ for the bearing.
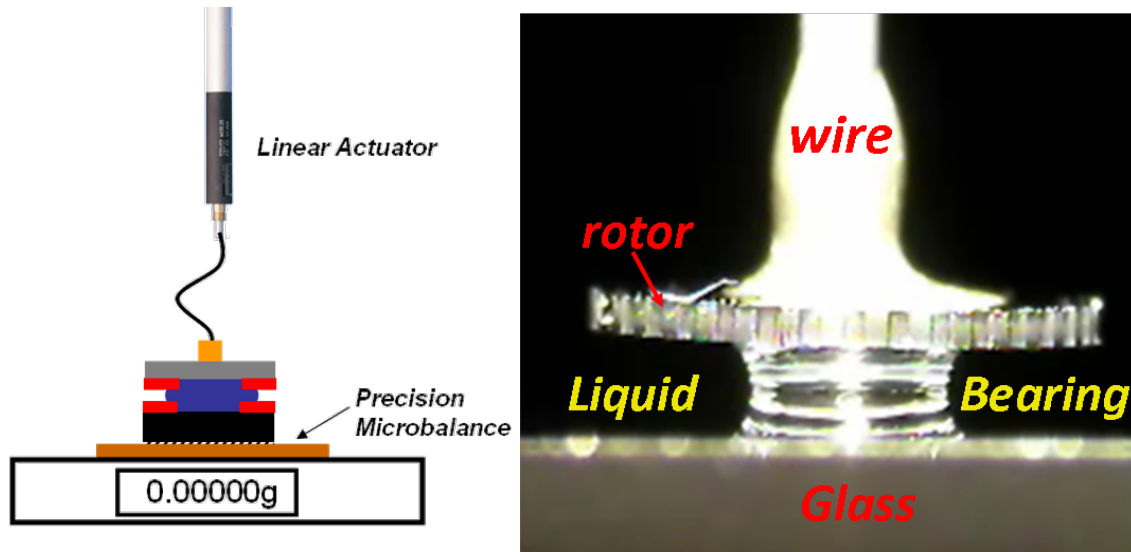
Fig. 26. Schematic diagram of the static load measurement test configuration is shown in the left figure. The liquid bearing assembly is placed on a precision microbalance, the rotor is connected to a linear actuation stage through a torque-free string, allowing direct force application in the vertical direction. The right image is a camera shot of the liquid bearing being placed in tension by the linear actuator motion during a test.

A schematic diagram of the test configuration is shown in Fig. 26. A quasi-static loading measurement using an electronic microbalance (A&D HR202i) with a sensitivity of 0.01 mg was conducted to determine both the tensile pull off force required to separate the rotor from the liquid surface and the compressive load carrying capability of the rotor. The assembled micromotor of the disk bearing design was placed inside the microbalance. Care was taken to run the experiment in a saturated vapor pressure environment by placing a beaker of supersaturated salt solution in the measuring chamber. The breeze break doors of the microbalance were closed or shielded to remove any air currents, and the experiments were run immediately after assembly to minimize any changes in liquid bearing volume due to evaporation. The rotor was attached to one end of a freely suspended string, while the other end was attached to a motorized linear actuator, (M230, Physik Instrumente) with a minimum step motion of 50 nm. Using a servo controller (C863 Mercury, Physik Instrumente), the rotor was lifted at a speed of 0.001 mm/s in a number of steps until the liquid bearing meniscus broke apart and the rotor was detached. At each translation step, the mass readout of the electronic balance was recorded after allowing the readout to stabilize. The retention force exerted by the liquid on the rotor is plotted against the relative displacement of the linear actuator in Fig. 27a) for liquid bearings with various volumes of ethylene glycol (EG).
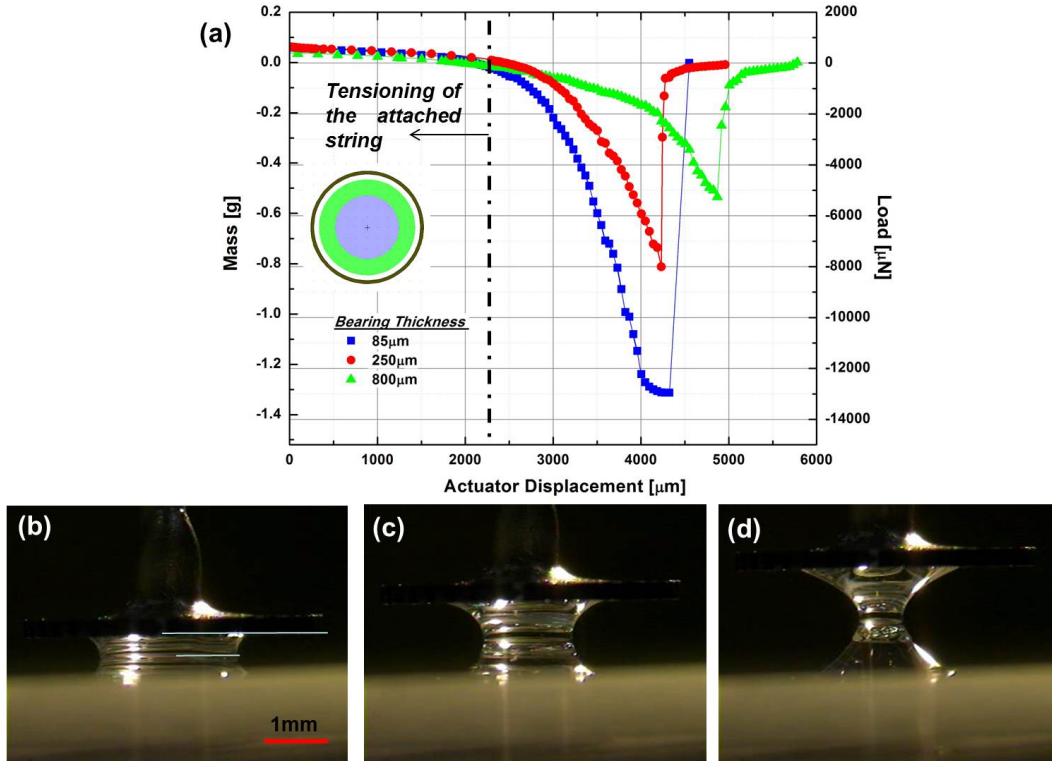
Fig. 27. (a) Static loading characteristics of the liquid bearing, Series of optical images taken as the liquid bearing is (b) loaded (c) deformed and (d) undergoing necking before breaking off.

Initially, the force readout remains unchanged as the actuator translates upwards, corresponding to tensioning of the string, as indicated by the inset figures. When the string is in tension, the tensile load is transferred to the bearing and deformation of the liquid bearing meniscus occurs as shown in Fig. 27b. The liquid bridge gradually necks (Fig. 27c) and eventually breaks off (Fig. 27d) as shown in the sudden change in force, indicating rotor pull off. The minimum of each curve indicates the maximum tensile load that the rotor can sustain which is highly dependent on the thickness of the bearing. For a bearing with 90 μm thickness, the pull off force is determined to be ~12.9mN.

In the small displacement regime, the experimental results agree with the analytical model described in Equation (4) within a factor of 2, a reasonable result given uncertainty about the initial bearing thickness and static contact angle. However, in the necking regime, the assumptions underlying the analytical model that the radii of the solid-liquid contact lines are very small compared to both the bearing radius, R and bearing height, g no longer holds true.

3.2.1.2   Dynamic Loading Measurements

To qualitatively examine the behavior of the bearing under dynamic loading, the rotor and bearing were assembled on a stator patterned at the end of a glass slide. The other end of the glass slide was mounted onto a clamp and an impulse hammer was used to excite the slide at the fixed end. The resulting acceleration of the rotor was computed by differentiating the velocity

measured using a Laser Doppler Vibrometer, LDV (Polytec). The results of experiments conducted with motor mounted in both the upright and inverted formats are shown in Fig. 28.
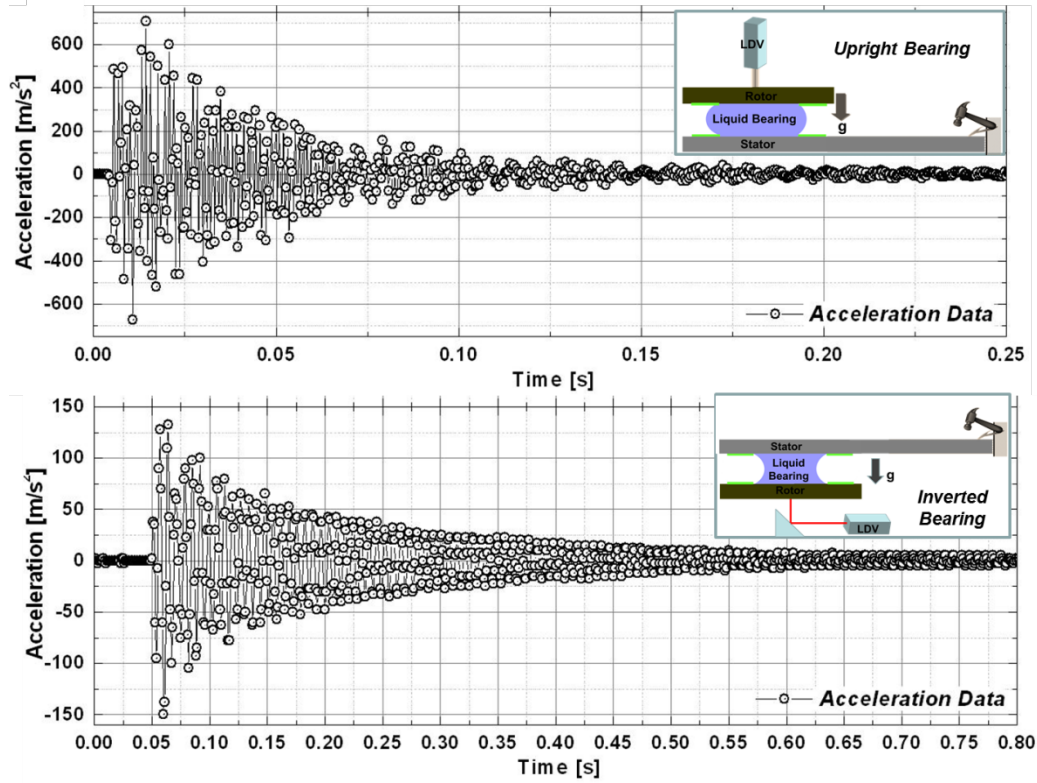

Fig. 28. Time response of the liquid bearing supported rotor under a random base excitation for (a) upright and (b) inverted configurations. Inset illustrates the test configuration.

The peak acceleration sustained by the upright and inverted micromotor are determined to be ~60g and ~15g respectively, where g denotes the gravitational acceleration equal to 9.81 m/s^2. These data points do not indicate the point of catastrophic failure, where the rotor detaches away from the stator. Safety considerations for the cantilevered stator forced limitation of the experimental input and only permitted measurement up to the values collected.

3.2.2   Torque Testing

Torque tests provide important information about bearing frictional performance. Two measurements are presented here that quantify the performance for low-speed and high-speed rotation. The low-speed measurement is referred to as startup torque and characterizes static sources of resistance to rotation, typically due to irregularities in the shape of the liquid bearing caused by defects or geometry issues in the surface coatings of the rotor and stator. The high-speed measurement presented is the maximum rotation rate as a function of input torque, and quantifies the dynamic resistance to rotation, typically due to shear forces in the central bearing or sliding drag friction from the satellite droplets.

3.2.2.1   Disk, Ring, and Full Bearing Startup Torque

Sources of friction and stiction that drive the startup torque measurement are difficult to quantify because they vary with surface defects, tension of the fluid, even the starting position of the rotor relative to the stator and relative to the magnetic field. As such, the data for startup torque tends to have a significant statistical deviation. Nonetheless, some important trends are discovered that provide insight into the strengths of each bearing design.

Startup torque, τ_s, is defined as the minimum $\tau_{applied}$ for the rotor to begin spinning. Fig. 29 shows experimental measurement of τ_s for different bearings geometries, fluid thicknesses and viscosities. The data show an exponential dependence on the fluid thickness, h. Moreover, the startup torque for the EG bearing is only slightly larger than that for H_2O, indicating that that fluid viscosity does not play an important role at slow rotation rates.
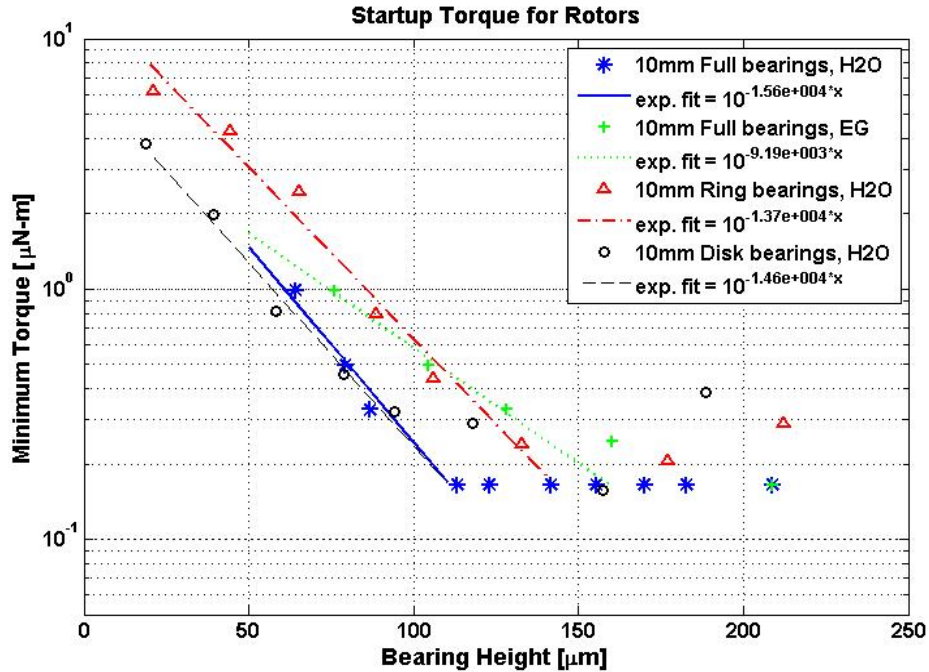

Fig. 29. Experimental data showing the trend of the startup torque with respect to varying bearing thickness and bearing geometries.

In the case of both ring and disk bearings, the bearing becomes less stable in tip/tilt as the thickness of the bearing increases. The edges of the tipping rotor contact the stator, resulting additional stiction and an increased startup torque. This tip/tilt instability is not apparent in the full coverage bearing, allowing the fluid bearing to operate with a thicker fluid layer. The start-up torque for the full bearing remains constant at 0.15 μN-m for fluid thickness $h > 120$ μm.

3.2.2.2 Satellite Bearing Startup Torque

The minimum startup torque was measured for the two stator coatings at a range of bearing thicknesses, as shown in Fig. 30. Variation in the startup torque data comes from initial conditions and positioning of the droplets interaction with the rough surface of the superhydrophobic coating. Measured mean values of startup torque are 0.315 µN-m for the optimized coating and 1.4 µN-m for the underpowered etched coating. These mean values match well with model predictions from Equation (14) based on Fig. 16 contact angle difference measurements of 10° and 44° respectively, and test parameters $R = 0.75$ mm, $n = 8$, $\gamma_{LV} = 72.8 \cdot 10^{-3}$ N/m, and $L_{SB} = 2.75$ mm.
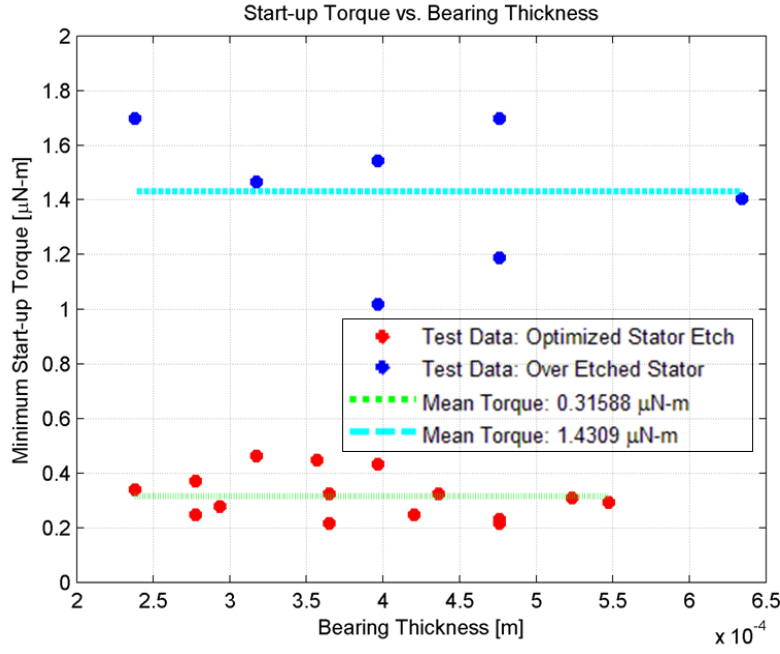

Fig. 30. Startup torque vs. Bearing thickness for an optimized stator coating and underpowered etched coating

3.2.2.3 Disk Bearing Rotational Drag Torque

For fluid bearings thicker than 100 µm, startup torque is small and bearing drag torque, is dominated by viscous drag torque, $\tau_v = b\Omega$, where Ω is the rotation rate and b is the viscous drag coefficient (defined in section III.B). When the friction is less than $\tau_{max} = \max(\tau_{applied}) = |m||B|$, increasing Ω increases drag and the phase angle, ϕ, approaches 90°. The critical rate of rotation occurs when $\tau_v = \tau_{max}$, above which the rotor oscillates at the excitation frequency but does not spin. Fig. 31. Experimental data showing the maximum rotation rate above which the rotor fails to follow the magnetic field. Measurements were conducted over different bearing thicknesses and magnetic torque levels to identify the parameters of the viscous friction model.

Fig. 48.shows that the maximum rotation rate depends linearly on both the liquid bearing thickness and the applied torque, consistent with the viscous friction model.

The mean viscous drag coefficient calculated experimentally as $b = |m||B|/\Omega_{max}$ for disk bearing designs from 110-150 µm thick, is 1.2×10^{-3} µN-m/rpm which is 20% higher than Equation (13) predicts using known values for the fluid viscosities. This result can be attributed to measurement uncertainty in the bearing thickness during torque measurements. The friction coefficient of the disk-type liquid bearing using H_2O as the fluid is approximately 15 times lower than that demonstrated in a micro-ball bearing supported rotor [6]. For an input torque of 1.6 µN-m, the maximum rotation rate as a function of the bearing thickness is calculated to be 0.225 rps/µm for the disk shaped H_2O bearing.
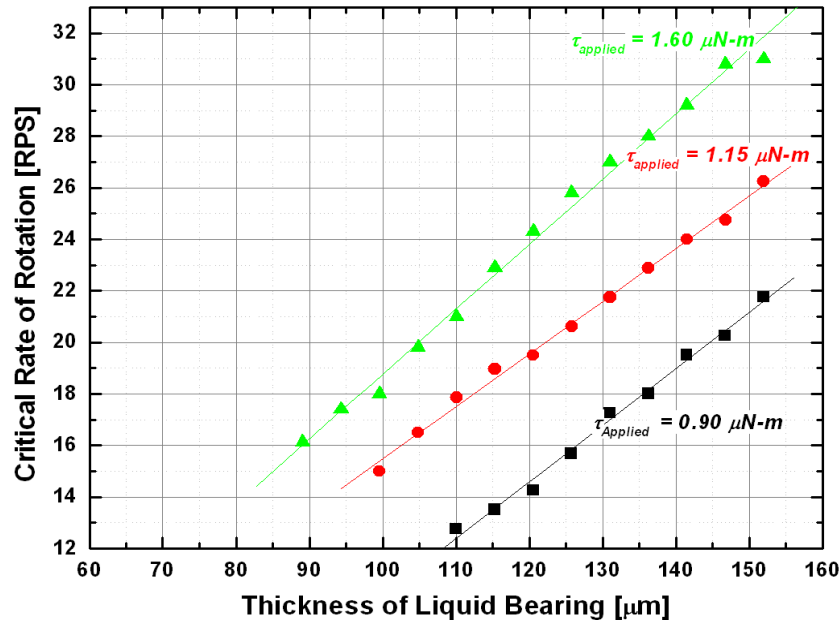
Fig. 31. Experimental data showing the maximum rotation rate above which the rotor fails to follow the magnetic field. Measurements were conducted over different bearing thicknesses and magnetic torque levels to identify the parameters of the viscous friction model.

In Fig. 31, for liquid bearings at ~145-150 µm thickness, with a $\tau_{applied}$ of 1.60 µN-m, the maximum rotation rate achieved was $\Omega_{max} = 30$ Hz, or 1800 rpm. Images of the rotor at rest, during spin up and at a constant rate of rotation of 1800 rpm are shown in Fig. 32. The rotors can be actuated in the upright mode as well as the inverted mode.

(a) Stationary   (b) Low Speed Rotation
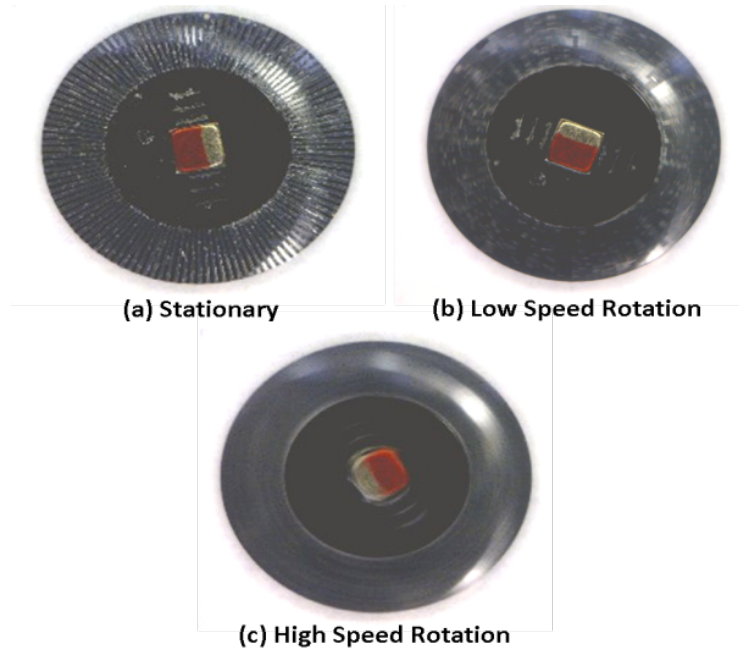
(c) High Speed Rotation

Fig. 32. Three video capture frames showing the magnetically actuated motor (a) at rest, (b) undergoing low speed rotation, and (c) rotating at a maximum rotation rate of 1800 rpm. When the motor is stationary, the etched markings at the circumference of the rotor are well defined. As the motor spins at higher speed, the rotational motion causes the markings to blur.

3.2.2.4   Satellite Bearing Drag Torque

Determination of the drag coefficient is based on the model described in Equation (14). Steady state drag torque, τ_{ss}, is a function of the bearing drag coefficient, b_{drag}, and the rotation rate, ω. The magnetic drive system torque is described in Equation (18), with a maximum drive torque achieved when the phase angle between the rotor and magnetic field is 90°. For this test, the steady state rotation rate is incrementally increased, until τ_{SS} exceeds $\tau_{applied}$, at which time the rotor ceases to rotation. The maximum rotation rate is plotted as a function of input torque in Fig. 33, for a 300 micron thick bearing. The slope of the linear data fit equates to $1/b_{drag}$. For the device measured, $b_{drag} = 0.94e\text{-}3$ µN-m/rpm, which is an improvement of 21% upon the result for a disk bearing presented previously.
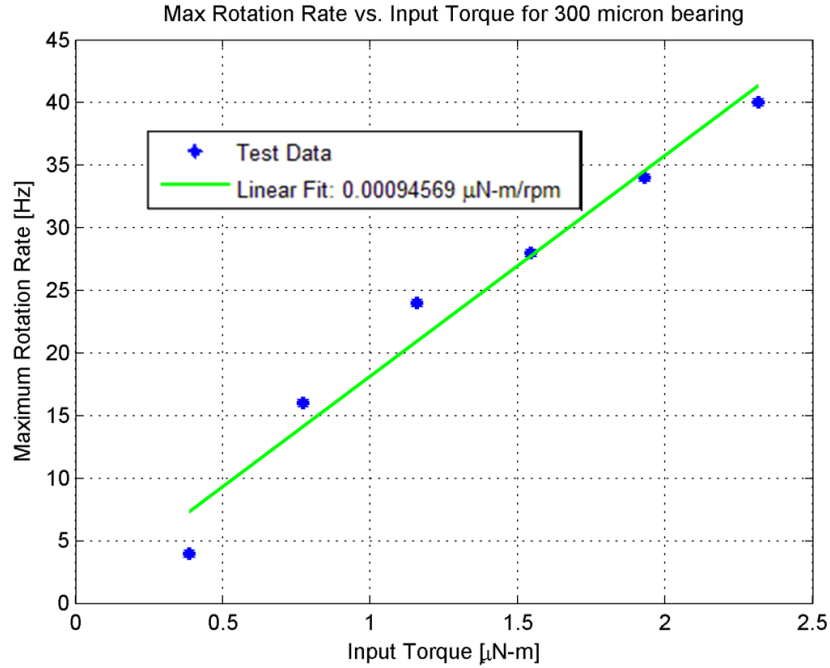
Fig. 33. Maximum rotation rate vs. input torque for a 300 μm thick bearing. Linear fit of the test data is $1/b_{drag}$ giving a drag coefficient of 0.94e-3 μN-m/rpm.

3.2.3 Tilt Stiffness

Tilt stiffness of the satellite bearing design corresponds to the load carrying capability of the system, and is especially relevant when considering alternative drive methods such as side-drive or top-drive electrostatic motors. To measure the stiffness, a tip/tilt torque was applied to the rotor using a magnetic field while the rotor tilt angle was measured optically. The maximum tilt angle vs. maximum torque for the test is plotted in Figure 29 for satellite bearings with a thickness of ~250 μm and surface patterned radius of 75 μm. The inverse slope of the linear data fit gives the tip/tilt stiffness, and is measured to be 5.4 μN-m/deg.

An analytical model as described in Equation (4) and Equation (13), for the geometry of the bearing described in the test data, is plotted against the test data in Fig. 34 and shows good agreement. Deviation between test data and model is due to non-ideal initial bearing volumes and excessive bearing deformation at high tilt angles.
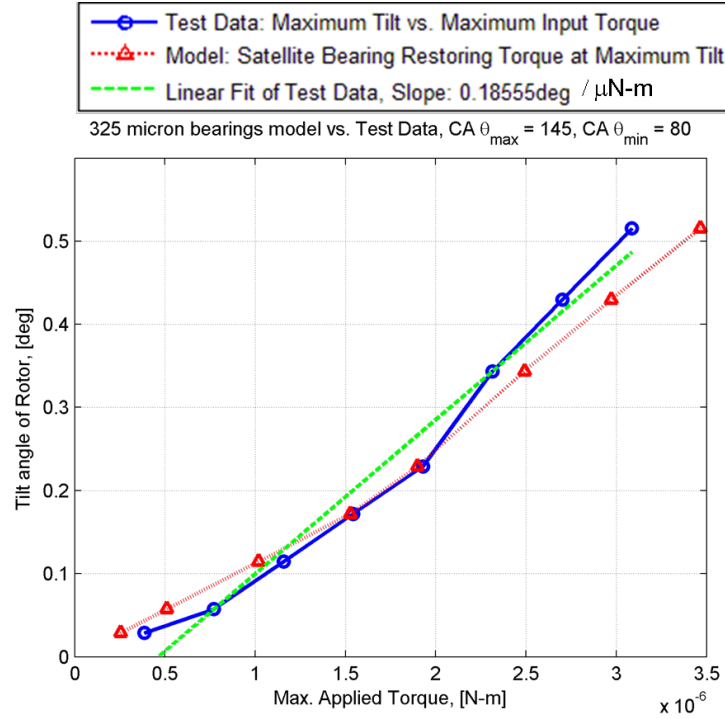
Fig. 34. Plots of test data, analytical model, and linear data fit for satellite bearing tip/tilt stiffness measurement.

3.2.4 Wobble

3.2.4.1 Full Bearing

Wobble is a measurement of the angular displacement of the rotor's normal axis relative to the stator's normal axis. Various effects contribute to wobble on a spinning liquid bearing rotor: 1) eccentricity error due to misalignment of the bearing with respect to rotor, 2) cogging due to surface defects at the edge of the bearing, 3) imbalanced magnetic torque due to the fact that the magnet's center is not coplanar with the liquid bearing, and 4) center of mass offset due to alignment error of the magnet mounted on the rotor. This last effect, misalignment of the magnet to the rotor which manifests itself as significant static rotor tilt, was the dominant error source observed in experiments.
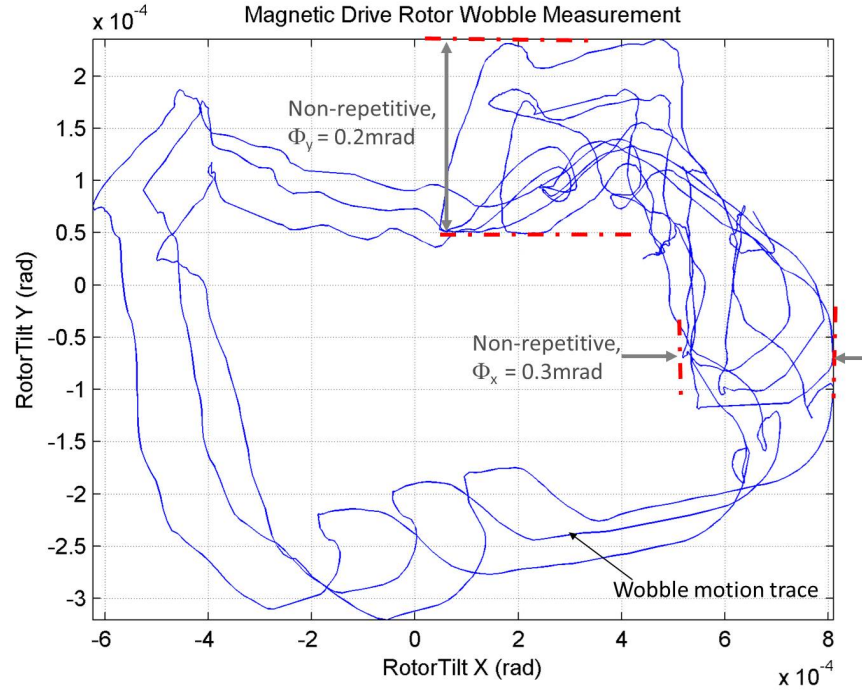
Fig. 35. Dynamic trajectory of the full bearing rotor spinning at a rotation rate of 500 rpm. The width of the full repetitive wobble trace is ~1.4mrad, while the non-repetitive component is shown to be ~0.3mrad.

To measure wobble in our system, a laser beam is reflected off the rotor surface at ~45° to the stator normal into a 2-axis position sensitive photodiode (PSD). The wobble trajectory of a full liquid bearing rotor spinning at speed of ~500 rpm is plotted for several revolutions in Fig. 35. The recorded data shows both a large 1.3 mrad repetitive component (due to static tilt of the rotor) as well as a smaller 0.3 mrad non-repetitive component.

For both the ring and disk bearings, the wobble is significant at all speeds. However, in the case of the full bearing, the wobble is only significant at low speeds (< 180 RPM). As described below, dynamic self-centering created at higher rotation rates by the circumferential fluid film helps to center the bearing and maintain a uniform gap between the rotor and stator, preventing contact and allowing smoother free rotation.

3.2.4.2   Satellite Bearing

Wobble was measured for the satellite bearing design using the same test setup as for the full bearing. Fig. 36shows the PSD data converted to angular tilt of the rotor. The sources of repeatable wobble in the satellite bearing are due to non-uniformity of satellite bearing deposition and irregularities in the stator surface. In the present assembly methodology, the satellite bearings are deposited manually using a micro-pipette capable of reliably placing drops larger than 5 microliters. The satellite droplets are close to 0.5 microliters, so accurate control of the deposition volume was challenging.

The repeatable wobble was measured at 5 mrad in the x-axis and 2 mrad in the y-axis. Non-repeatable wobble derives from the roughness in the stator and vibration of the rotor on the

bearings. While the repeatable wobble may be improved by better deposition accuracy of the bearing droplets, the non-repeatable wobble is due to sources which will ultimately affect the performance of the rotational platform. Non-repeatable wobble was measured at 0.3 mrad and 0.3 mrad in the x and y rotational axes, respectively.

Wobble measurements between the satellite bearing design and the full bearing measurements are compared in Fig. 37. The repeatable wobble measurement for the satellite bearing is significantly larger than for the full bearing, but the non-repeatable measurement is very comparable.
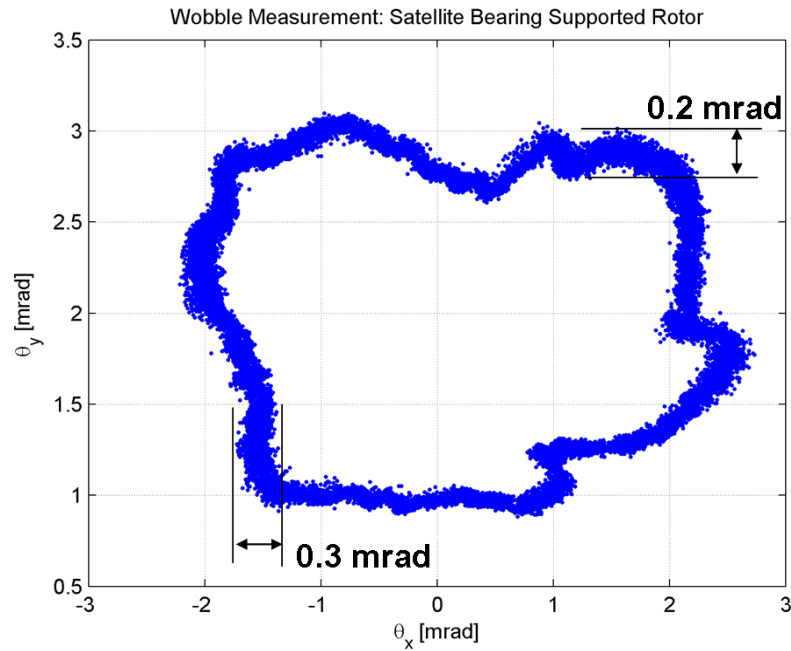

Fig. 36. Wobble measurement for the satellite bearing design. Repeatable wobble measurements are the extents of the wobble trace. The non-repeatable measurement is the width of the trace. For the satellite bearing, the repeatable wobble is 5 mrad and 3 mrad in x and y respectively, non-repeatable wobble is 0.3 mrad and 0.2 mrad in x and y respectively.
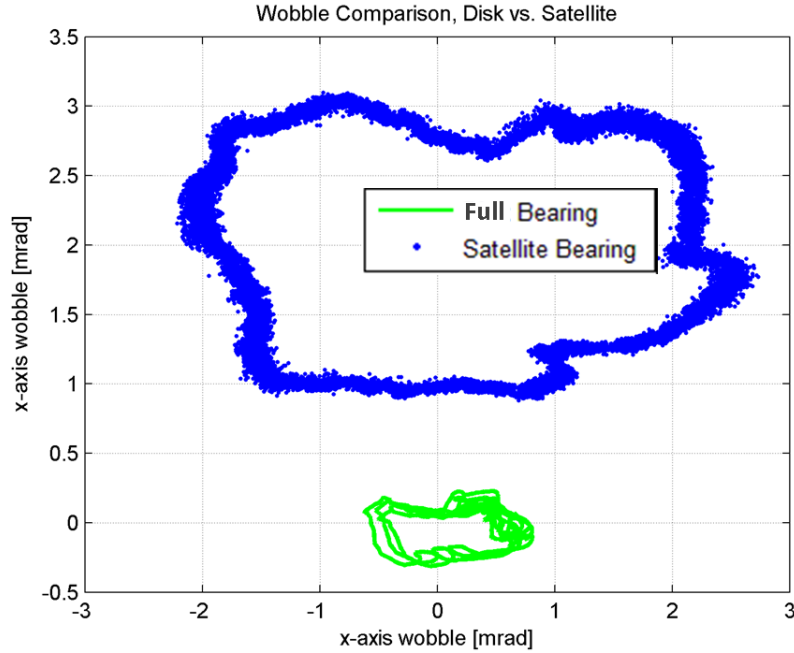
Fig. 37. Comparison of the wobble traces for the satellite bearing supported rotor and full bearing supported rotor. The repeatable wobble is significantly higher for the satellite design, due to volume differences in the satellite droplets, but the non-repeatable wobble is very similar.

3.2.4.3   Mechanical Resonances

The disk, ring, and satellite bearing designs exhibited resonant oscillation when rotating at certain frequencies, as the center of gravity (CG) imbalance interacted with the effective lateral spring constant of the liquid bearing. The primary source of CG imbalance is inaccurate placement of the magnet during rotor assembly, but minor sources from the micro-lithography fabrication process also exist. Generally the alignment capability during micro-lithography is several micrometers through microscope based visual alignment using micrometer stages to overlay reference marks. The alignment of the magnet to rotor is accomplished manually with no magnification, so misalignment on the order of several hundred microns is often seen.

The lateral restoring force described in Section 2.3 provides an effective spring constant in the liquid bearing. No direct measurement of the lateral spring constant was taken. The spring constant is a function of bearing thickness, the surface tension of the fluid, and the surface energy and advancing/receding contact angles of the hydrophobic coatings on both the rotor and stator surfaces.

Observational data from using CG misaligned rotor assemblies during testing indicate that for mildly misaligned magnets of less than approximately 100 μm, the resonance was not of sufficient amplitude or at a frequency that affected operation of the device. For magnets with misalignment on the order of 0.5 mm, however the resonances were observed between 5 and 16 Hz rotation rate, and if the rotor was allowed to spin at the resonance for a few seconds, the

magnitude of sideways wobble was sufficient to overcome the liquid bearing restoring force, causing the rotor to slide off the stator. The resonant failure mode only occurred for disk, ring, and satellite bearing designs, while the full bearing exhibited self-centering stability at all rotational velocities.

3.2.5   Self-centering of Full Bearing

Noticeable self-centering of the full bearing supported rotor during start-up torque tests led to characterization of the centering effect. The rotational test bed was modified to operate with the rotor normal vector at various tilt angles, ϕ, relative to gravity, G, providing a de-centering force on the rotor, $F_{decenter}$, as a function of the rotor mass, m:

$$F_{decenter} = m\, G \sin(\phi) \tag{19}$$

The self-centering is quantified using the eccentricity, e, which is the distance between the rotor and stator centers, and can vary between 0 and the clearance, C, which is the distance between rotor edge and stator wall when $e = 0$. An alternative measurement is $h_{min} = C\text{-}e$, the minimum distance between rotor edge and stator for a given e. The normalized eccentricity is $\varepsilon = e/C$ and is related to h_{min} by $h_{min} = C(1\text{-}\varepsilon)$.

Measured eccentricity as a function of tilt angle and rotation rate is displayed in Fig. 38. When the motor is level, $\phi = 0$, and self-centering is complete at all rotation rates, Ω. However, when the motor is not level, the decentering force is non-zero and a threshold Ω must be achieved before h_{min} rises above zero and the rotor separates from the stator wall.

Several models were investigated to explain the observed self-centering effect of the full-bearing configuration. The rotation rate dependence suggested an analogy to a journal bearing [58, 59], where a fluid film between the rotor and stator walls builds up a pressure differential with rotational velocity, providing a force counter to $F_{decenter}$ that separates the two bodies. Analytical and computational models of journal bearing performance under-predicted the observed centering effect by several orders of magnitude, predicting a separation h_{min} of only a fraction of a micrometer at rotation rates below 30 Hz. A second model was developed by accounting for energy loss from friction drag, and noting that the rotor would move to the position with the smallest energy loss.
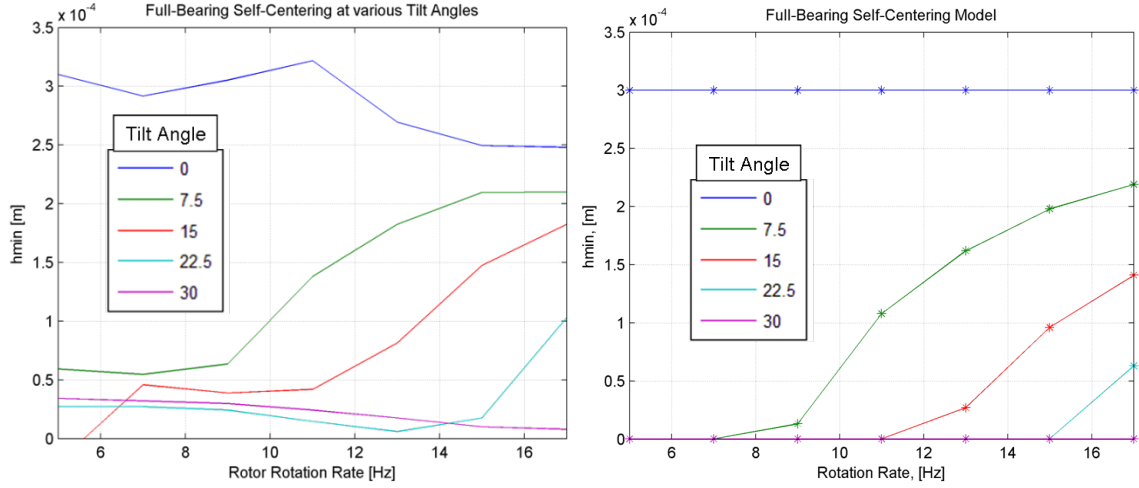
Fig. 38. (a) Measurement of eccentricity vs. rotation rate and liquid bearing tilt angle. (b) Model of eccentricity vs. rotation rate and liquid bearing tilt angle.

The self-centering model which most closely matches the test data minimizes the total energy in the system, with kinetic energy calculated for the rotating liquid bearing and potential energy as a function of rotor eccentricity as shown in Equation (20).

$$
\begin{aligned}
E_{total} &= E_k + E_p \\
&= \sum_i \iiint_{r_i, \theta_i, z_i} \rho_{LB} r^2 \cdot r \, dr \, d\theta \, dz + \left(\left(\rho_{Si} - \rho_{LB} \right) \pi R_{rotor}^2 t + m_{magnet} \right) \cdot G \cdot e \sin(\phi)
\end{aligned}
\tag{20}
$$

where ρ_{LB} and ρ_{Si} are densities of the liquid bearing fluid and silicon respectively, m_{magnet} is the mass of the magnet, r, θ and z are integration parameters (radial distance from rotor center, angle around rotor, and height above stator respectively) and the summation term i results from performing the integration over different regions of liquid bearing.

Energy calculations for various rotation rates plotted as a function of eccentricity in a 7.5 deg tilt configuration, with marks on the curves at the minimum energy positions are shown in Fig. 39. The minimum energy positions from Fig. 39are plotted as the 7.5 deg tilt line in simulated eccentricity data in Figure 34b. Similar plots were created using the energy model for tilt angles from 0 to 30 degrees and good agreement is observed between the experimentally measured eccentricity, Fig. 38a, and the simulated eccentricity predicted using the energy model, Fig. 38b.
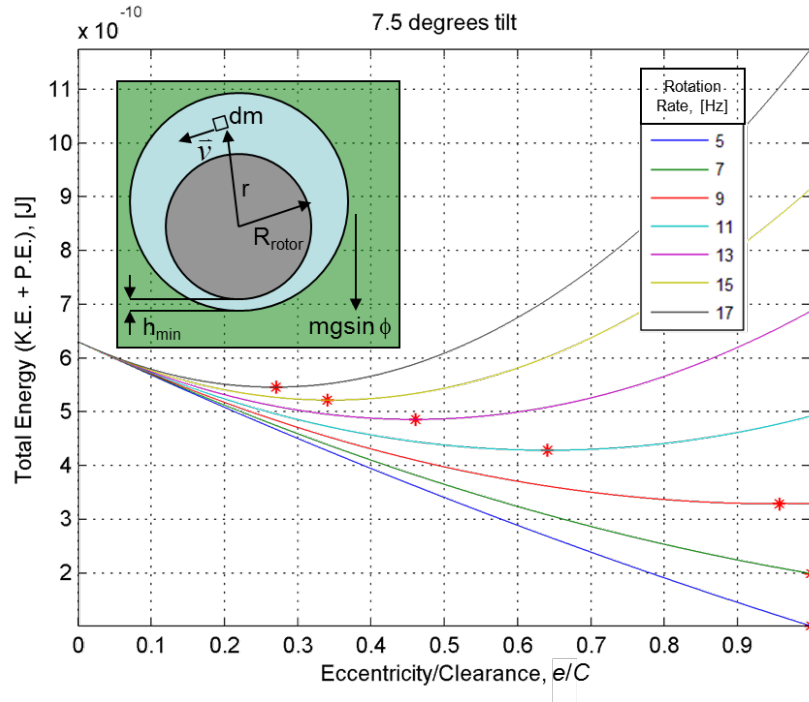
Fig. 39. Total energy (including kinetic energy and potential energy) of the rotor and liquid bearing system for rotation rates between 5 and 17 Hz rotation rate plotted vs. rotor eccentricity. The minimum energy positions are indicated on each curve.

3.3 Discussion

Previously reported rotary micromotors that operated without any solid-solid contact between rotor and stator have been limited in their operating range or through their use of actively controlled centering mechanisms. Table 5 shows the relationship between bearing centering forces and the operating space for each of them. The surface tension based liquid bearing technology is the only non-controlled method that provides static centering capability. Both surface tension based and minimum energy based designs [14] provide centering at low rotation rates. Externally pressurized gas bearings [7] operate in a range from tens of rpm to very high rotation rates. Magnetic and electrostatic [8, 9] supported air bearing rotary motors operate at a range of rotation speeds, but actively controlled fields are required for stability introduce complexity in implementation.
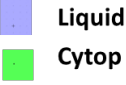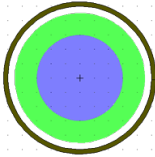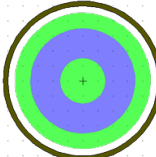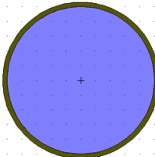
Table 5: Operating space for contact-free rotary micromotor bearing designs based on the method used to provide centering of the rotor relative to the stator.

Non Solid-Solid Interface Rotary Micromotors					
Bearing Design		Operating Space (Rotation Speed)			
	Centering Force	Static	Low (<1 rpm)	Med (<10^3rpm)	High (<10^6rpm)

Passive Methods	Surface Tension	X	X		
	Min Energy		X	X	
	Externally Pressurized Gas			X	X
Active Methods	Magnetic	X	X	X	
	Electrostatic	X	X	X	

An ideal micromotor bearing design will cover the operating space, providing passive positioning capability free from solid-solid friction and wear that allows operation from zero to 10^6 rpm and higher rotation rates. To date, no device is able to achieve all the desired characteristics.

Table 6: Summary of liquid bearing designs tested in this work.
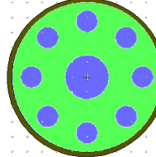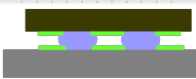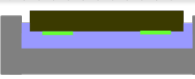
Bearing Design	Disk Bearing	Ring Bearing	Full Bearing	Satellite Bearing
Top View of Bearing — Liquid / Cytop				
X-Section of Bearing	rotor / stator			
Rotor Radius [mm]	5	5	5	5
Bearing Radius [mm]	3	Inner = 1.5, Outer = 3.5	5	Central = 1; Satellite = 0.5
Startup-Torque [μN-m]	0.2	0.25	0.15	0.3
Wobble [mrad]	High	High	0.3	0.3
Drag Coeff. [μNm/rpm]	1.2e-3	-	1.12e-3	**0.94e-3**
Max. Rotation Rate [deg/s]	10,080	9780	10,800	**14,400**
Pos Stable	Yes	Yes	No	Yes
Tilt Stable	No	No	No	Yes

Liquid bearing technology extends the operating space of rotary micromotors by providing low-friction, wear-free, passive, stable translational, piston, and tilt mode reference between rotor and

stator, all in a design with no solid-solid interfaces. By eliminating sliding and rolling friction forces, the performance of the technology is improved compared with other friction reduction methods in the static to medium-rpm operating range. The liquid bearings that were designed, fabricated, characterized, and discussed in this work are summarized in Table 6.

The disk bearing was characterized to have minimum startup torque at 0.2 μN-m, a rotational drag coefficient of $1.2 \cdot 10^{-3}$ μN-m/rpm, and a maximum rotation rate of 10,080 deg/sec for an input torque of 1.6 μN-m. The measured drag coefficient matched the model prediction. The ring bearing performance was very similar to the disk bearing. Both the disk and ring bearing designs had significant wobble of the rotor relative to the stator due to instability in tip and tilt.

The full bearing was characterized to have a minimum startup torque of 0.15 μN-m and a maximum rotation rate of 10,800 deg/sec. The rotational drag coefficient was measured to be $1.12 \cdot 10^{-3}$ μN-m/rpm. The full bearing design was unstable in position and tip/tilt modes when not rotating, but once rotation was initiated, dynamic self-centering and flattening of the rotor was demonstrated so that wobble measurement was possible. Wobble for the full bearing was measured at 0.3 mrad of non-repeatable motion.

The satellite droplet liquid bearing was characterized to have minimum startup torque at 0.3 μN-m, rotational drag coefficient at $0.94 \cdot 10^{-3}$ μN-m/rpm, and maximum rotation rate at 14400 deg/sec for an input torque of 2.3 μN-m. The measured drag and start-up torque agree well with the predictions of a model based on surface tension forces on the liquid droplets.

Tilt stability and stiffness are especially important factors that must be considered during drive mechanism selection and design. The tilt stiffness of the satellite bearing design was measured at 5.4 μN-m/deg. Tilt stiffness measurement and analytical models provide the design tools needed for predicting pull-in instability threshold gaps and voltages.

Two SHP coatings are demonstrated and characterized in this work. The rotor SHP coating consists of micropatterned Si pillars coated with the amorphous fluoropolymer Cytop that is compatible with subsequent wafer processing and achieves a static contact angle of 156° and advancing and receding contact angles of 166.0° and 162.5° respectively. The stator uses a laser-roughened PDMS coating to achieve a static contact angle of 162° and advancing and receding angles of 10° and 20° respectively. The SHP coatings are critical to the ability of liquid bearings to provide alignment in five axes (x/y translation, piston, tip, and tilt) while allowing low operating friction in the rotational axis of the motor.

4. References

[1]   L.-S. Fan, Y.-C. Tai, and R. S. Muller, "IC-processed electrostatic micromotors," *Sensors and Actuators,* vol. 20, pp. 41-47, Nov. 1989.

[2]   M. Mehregany, S. F. Bart, L. S. Tavrow, J. H. Lang, S. D. Senturia, and M. F. Schlecht, "A study of three microfabricated variable-capacitance motors," *Sensors and Actuators A: Physical,* vol. 21, pp. 173-179, Feb. 1990.

[3]   V. Kaajakari, S. Rodgers, and A. Lal, "Ultrasonically driven surface micromachined motor," in *Micro Electro Mechanical Systems, 2000. MEMS 2000. The Thirteenth Annual International Conference on*, 2000, pp. 40-45.

[4]   P. Muralt, "Ultrasonic Micromotors Based on PZT Thin Films," *Journal of Electroceramics,* vol. 3, pp. 143-150, 1999.

[5]   C. H. Ahn, Y. J. Kim, and M. G. Allen, "A planar variable reluctance magnetic micromotor with fully integrated stator and coils," *Journal of Microelectromechanical Systems,* vol. 2, pp. 165-173, Dec. 1993.

[6]   N. Ghalichechian, A. Modafe, M. I. Beyaz, and R. Ghodssi, "Design, Fabrication, and Characterization of a Rotary Micromotor Supported on Microball Bearings," *Journal of Microelectromechanical Systems,* vol. 17, pp. 632-642, Jun. 2008.

[7]   L. G. Fréchette, S. A. Jacobson, K. S. Breuer, F. F. Ehrich, R. Ghodssi, R. Khanna, C. W. Wong, X. Zhang, M. A. Schmidt, and A. H. Epstein, "High-speed microfabricated silicon turbomachinery and fluid film bearings," *Journal of Microelectromechanical Systems,* vol. 14, pp. 141-152, Feb. 2005.

[8]   S. Kumar, D. Cho, and W. N. Carr, "Experimental study of electric suspension for microbearings," *Journal of Microelectromechanical Systems,* vol. 1, pp. 23-30, Mar. 1992.

[9]   X. S. Wu, W. Y. Chen, X. L. Zhao, and W. P. Zhang, "Micromotor with electromagnetically levitated rotor using separated coils," *Electronics Letters,* vol. 40, pp. 996-997, Aug 2004.

[10]   M. McCarthy, C. M. Waits, and R. Ghodssi, "Dynamic Friction and Wear in a Planar-Contact Encapsulated Microball Bearing Using an Integrated Microturbine," *Microelectromechanical Systems, Journal of,* vol. 18, pp. 263-273, Apr. 2009.

[11]   B. Wagner, M. Kreutzer, and W. Benecke, "Permanent magnet micromotors on silicon substrates," *Microelectromechanical Systems, Journal of,* vol. 2, pp. 23-29, Feb. 1993.

[12]   T. Asada, H. Saitou, Y. Asaida, and K. Itoh, "Characteristic analysis of hydrodynamic bearings for HDDs," in *Asia-Pacific Magnetic Recording Conference, 2000. APMRC 2000,* 2000, pp. MA6/1-MA6/2.

[13]   A. Takei, N. Binh-Khiem, E. Iwase, K. Matsumoto, and I. Shimoyama, "Liquid motor driven by electrowetting," in *2008 21st IEEE International Conference on Micro Electro Mechanical Systems - MEMS '08*, Tucson, AZ,, 2008, pp. 42-45.

[14]   M. L. Chan, B. Yoxall, H. Park, Z. Kang, I. Izyumin, J. Chou, M. M. Megens, M. C. Wu, B. E. Boser, and D. A. Horsley, "Low friction liquid bearing mems micromotor," in *Micro Electro Mechanical Systems (MEMS), 2011 IEEE 24th International Conference on*, 2011, pp. 1237-1240.

[15]   W. S. N. Trimmer and K. J. Gabriel, "Design considerations for a practical electrostatic micro-motor," *Sensors and Actuators,* vol. 11, pp. 189-206, 1987.

[16]   L.-S. Fan, Y.-C. Tai and R.S.Muller, "IC-processed electrostatic micromotors," presented at the *International Electronics Devices Meeting* San Francisco, CA, U.S.A., 1988.

[17]   Y.-C. Tai and R. S. Muller, "IC-processed electrostatic synchronous micromotors," *Sensors and Actuators,* vol. 20, pp. 49-55, 1989.

[18]   Y.-C. Tai and R. S. Muller, "Frictional study of IC-processed micromotors," *Sensors and Actuators A: Physical,* vol. 21, pp. 180-183, 1990.

[19]   M. Mehregany, S. F. Bart, L. S. Tavrow, J. H. Lang, and S. D. Senturia, "PRINCIPLES IN DESIGN AND MICROFABRICATION OF VARIABLE-CAPACITANCE SIDE-DRIVE MOTORS," *Journal of Vacuum Science & Technology a-Vacuum Surfaces and Films,* vol. 8, pp. 3614-3624, Jul-Aug 1990.

[20]   M. Mehregany, S. D. Senturia, and J. H. Lang, "Friction and wear in microfabricated harmonic side-drive motors," in *Solid-State Sensor and Actuator Workshop, 1990. 4th Technical Digest., IEEE*, 1990, pp. 17-22.

[21]   M. G. Lim, J. C. Chang, D. P. Schultz, R. T. Howe, and R. M. White, "Polysilicon microstructures to characterize static friction," in *Micro Electro Mechanical Systems, 1990. Proceedings, An Investigation of Micro Structures, Sensors, Actuators, Machines and Robots. IEEE*, 1990, pp. 82-88.

[22]   U. Beerschwinger, R. L. Reuben, and S. J. Yang, "Frictional study of micromotor bearings," *Sensors and Actuators a-Physical,* vol. 63, pp. 229-241, Dec 1997.

[23]   W. Zhang, G. Meng, and H. Li, "Electrostatic micromotor and its reliability," *Microelectronics Reliability,* vol. 45, pp. 1230-1242, 2005.

[24]   E. S. Piekos and K. S. Breuer, "Pseudospectral Orbit Simulation of Nonideal Gas-Lubricated Journal Bearings for Microfabricated Turbomachines," *Journal of Tribology,* vol. 121, pp. 604-609, 1999.

[25]   F. F. Ehrich and S. A. Jacobson, "Development of High-Speed Gas Bearings for High-Power Density Microdevices," New Orleans, LA (USA), 2003, pp. 141-148.

[26]   K. Matsuoka, S. Obata, H. Kita, and F. Toujou, "Development of FDB spindle motors for HDD use," *2000 Asia-Pacific Magnetic Recording Conference. Digests of APMRC2000 on Mechanical and Manufacturing Aspects of HDD (Cat. No.00EX395),* pp. MA1/1-MA1/2MA1/2, 2000 2000.

[27]   G. Fuhr, R. Hagedorn, T. Muller, W. Benecke, U. Schnakenberg, and B. Wagner, "DIELECTRIC INDUCTION MICROMOTORS - FIELD LEVITATION AND TORQUE FREQUENCY-CHARACTERISTICS," *Sensors and Actuators a-Physical,* vol. 32, pp. 525-530, Apr 1992.

[28] L.-H. Lu, R. Kee Suk, and L. Chang, "A magnetic microstirrer and array for microfluidic mixing," *Microelectromechanical Systems, Journal of,* vol. 11, pp. 462-469, 2002.

[29] A. A. Darhuber and S. M. Troian, "Principles of microfluidic actuation by modulation of surface stresses," *Annual Review of Fluid Mechanics,* vol. 37 pp. 425-455, 2005.

[30] M. G. Pollack, R. B. Fair, and A. D. Shenderov, "Electrowetting-based actuation of liquid droplets for microfluidic applications," *Applied Physics Letters,* vol. 77, pp. 1725-1726, Sep. 2000.

[31] M. G. Pollack, A. D. Shenderov, and R. B. Fair, "Electrowetting-based actuation of droplets for integrated microfluidics," *Lab on a Chip,* vol. 2, pp. 96-101, 2002.

[32] V. Srinivasan, V. K. Pamula, and R. B. Fair, "An integrated digital microfluidic lab-on-a-chip for clinical diagnostics on human physiological fluids," *Lab on a Chip,* vol. 4, pp. 310-315, 2004.

[33] T. B. Jones, "On the Relationship of Dielectrophoresis and Electrowetting," *Langmuir,* vol. 18, pp. 4437-4443, 2002.

[34] A. A. Darhuber, J. P. Valentino, S. M. Troian, and S. Wagner, "Thermocapillary actuation of droplets on chemically patterned surfaces by programmable microheater arrays," *Microelectromechanical Systems, Journal of,* vol. 12, pp. 873-879, 2003.

[35] U. Srinivasan, M. A. Helmbrecht, C. Rembe, R. S. Muller, and R. T. Howe, "Fluidic self-assembly of micromirrors onto microactuators using capillary forces," *Selected Topics in Quantum Electronics, IEEE Journal of,* vol. 8, pp. 4-11, 2002.

[36] U. Srinivasan, D. Liepmann, and R. T. Howe, "Microstructure to substrate self-assembly using capillary forces," *Microelectromechanical Systems, Journal of,* vol. 10, pp. 17-24, 2001.

[37] S. Abbasi, A. X. Zhou, R. Baskaran, and K. F. Bohringer, "Part tilting in capillary-based self-assembly: Modeling and correction methods," presented at the *Micro Electro Mechanical Systems, 2008. MEMS 2008. IEEE 21st International Conference on*, 2008.

[38] A. Kajiwara, K. Suzuki, H. Miura, and H. Takanobu, "Study on micromotor using surface tension of liquid droplets," *Research Reports of Kogakuin University,* pp. 25-30, October 2006.

[39] J. Lee and K. Chang-Jin, "Surface-tension-driven microactuation based on continuous electrowetting," *Microelectromechanical Systems, Journal of,* vol. 9, pp. 171-180, 2000.

[40] P.-G. De Gennes, F. Brouchard-Wyart, and D. Quere, *Capillarity and Wetting Phenomena: Drops, Bubbles, Pearls, and Waves*: Springer, 2003.

[41] M. A. Fortes, "Axisymmetric liquid bridges between parallel plates," *Journal of Colloid and Interface Science,* vol. 88, pp. 338-352, Aug. 1982.

[42] P. Lambert, A. Chau, A. Delchambre, and S. Regnier, "Comparison between Two Capillary Forces Models," *Langmuir,* vol. 24, pp. 3157-3163, Apr. 2008.

[43] M. Mastrangeli and et al., "Lateral capillary forces of cylindrical fluid menisci: a comprehensive quasi-static study," *Journal of Micromechanics and Microengineering,* vol. 20, p. 075041, Jul. 2010.

[44] R. Maboudian and R. T. Howe, "Critical review: Adhesion in surface micromechanical structures," *Journal of Vacuum Science & Technology B,* vol. 15, pp. 1-20, Jan-Feb 1997.

[45] U. Srinivasan, M. R. Houston, R. T. Howe, and R. Maboudian, "Alkyltrichlorosilane-based self-assembled monolayer films for stiction reduction in silicon micromachines," *Journal of Microelectromechanical Systems,* vol. 7, pp. 252-260, Jun 1998.

[46] D. C. Tretheway and C. D. Meinhart, "Apparent fluid slip at hydrophobic microchannel walls," *Physics of Fluids,* vol. 14, pp. L9-L12, Mar 2002.

[47] C. Cottin-Bizonne, J. L. Barrat, L. Bocquet, and E. Charlaix, "Low-friction flows of liquid at nanopatterned interfaces," *Nature Materials,* vol. 2, pp. 237-240, Apr. 2003.

[48] R. N. Wenzel, "Resistance of solid surfaces to wetting by water," *Industrial and Engineering Chemistry,* vol. 28, pp. 988-994, Aug. 1936.

[49] A. B. D. Cassie and S. Baxter, "Wettability of porous surfaces," *Transactions of the Faraday Society,* vol. 40, pp. 546-550, 1944.

[50] D. Öner and T. J. McCarthy, "Ultrahydrophobic Surfaces. Effects of Topography Length Scales on Wettability," *Langmuir,* vol. 16, pp. 7777-7782, Oct. 2000.

[51] L. Zhu, Y. Feng, X. Ye, and Z. Zhou, "Tuning wettability and getting superhydrophobic surface by controlling surface roughness with well-designed microstructures," *Sensors and Actuators A: Physical,* vol. 130-131, pp. 595-600, Aug. 2006.

[52] B. Bhushan and Y. C. Jung, "Wetting study of patterned surfaces for superhydrophobicity," *Ultramicroscopy,* vol. 107, pp. 1033-1041, Oct. 2007.

[53] L. Hong and T. Pan, "Photopatternable Superhydrophobic Nanocomposites for Microfabrication," *Journal of Microelectromechanical Systems,* vol. 19, pp. 246-253, Apr. 2010.

[54] M. Nosonovsky and B. Bhushan, "Superhydrophobic surfaces and emerging applications: Non-adhesion, energy, green engineering," *Current Opinion in Colloid & Interface Science,* vol. 14, pp. 270-280, Aug. 2009.

[55] K. K. S. Lau, J. Bico, K. B. K. Teo, M. Chhowalla, G. A. J. Amaratunga, W. I. Milne, G. H. McKinley, and K. K. Gleason, "Superhydrophobic carbon nanotube forests," *Nano Letters,* vol. 3, pp. 1701-1705, Dec 2003.

[56] L. B. Zhu, Y. H. Xiu, J. W. Xu, P. A. Tamirisa, D. W. Hess, and C. P. Wong, "Superhydrophobicity on two-tier rough surfaces fabricated by controlled growth of aligned carbon nanotube arrays coated with fluorocarbon," *Langmuir,* vol. 21, pp. 11208-11212, Nov. 2005.

[57] K. Brakke. (2008, Sept.). *The Surface Evolver (2.30 ed.).* Available: http://www.susqu.edu/brakke/evolver/evolver.html

[58] M. M. Khonsari and E. R. Booser, *Journal Bearings*: John Wiley & Sons, Ltd, 2008.

[59] E. Piekos, "Numerical simulation of gas-lubricated journal bearings for microfabricated machines," Ph.D. Doctoral thesis, MIT, Cambridge, MA, USA, 2000.